Air Mass Transport to the Tropical West Pacific Troposphere inferred from Ozone and Relative Humidity Balloon Observations above Palau

Katrin Müller[1], Peter von der Gathen[1], and Markus Rex[1,2]

[1]Alfred-Wegener-Institute, Helmholtz Center for Polar and Marine Research, Telegrafenberg A45, 14473 Potsdam, Germany
[2]Universität Potsdam, Institut für Physik und Astronomie, Potsdam, Germany

Correspondence: Katrin Müller (katrin.mueller@awi.de)

Abstract.

The transport history of tropospheric air masses above the tropical West Pacific (TWP) is reflected by the local ozone and relative humidity (RH) characteristics. In boreal winter, the TWP is the main global entry point for air masses into the stratosphere and therefore a key region of atmospheric chemistry and dynamics. Our study aims to identify air masses with different pathways to the TWP using ozone and radio soundings from Palau from 2016-2019. Supported by backward trajectory calculations, we found five different types of air masses. We further defined locally controlled ozone and RH background profiles based on monthly statistics and analyzed corresponding anomalies in the 5–10 km altitude range. Our results show a bimodality in RH anomalies. Humid and ozone-poor background air masses are of local or Pacific convective origin and occur year-round, but dominate from August until October. Anomalously dry and ozone-rich air masses indicate a non-local origin in Tropical Asia and are transported to the TWP via an anticyclonic route, mostly from February to April. The geographic location of origin suggests anthropogenic pollution or biomass burning as a cause for ozone production. We propose large-scale descent within the tropical troposphere and radiative cooling in connection with the Hadley circulation as being responsible for the dehydration during transport. The trajectory analysis revealed no indication of a stratospheric influence. Our study thus presents a valuable contribution to the discussion about anomalous layers of dry ozone-rich air observed in ozone-poor background profiles in the TWP.

1 Introduction

The Tropical West Pacific (TWP), an area extending from the Maritime Continent to the International Date Line, is considered the major air mass transport pathway from the troposphere to the stratosphere during boreal winter (e.g., Newell and Gould-Stewart, 1981; Fueglistaler et al., 2004; Krüger et al., 2008). Air masses entering the stratosphere largely originate in the local TWP boundary layer and free troposphere (Rex et al., 2014). Thus, the local tropospheric air composition has a key impact on concentrations of various chemical species within the global stratosphere, even up to a potential impact on polar ozone depletion.

Understanding (1) the variability of composition and transport of air masses to this region as well as (2) the unique air chemistry are therefore of great relevance. The monitoring of tropospheric ozone (O_3) concentrations sheds light on both aspects: (1) O_3 is a chemical tracer for both local convective ("low" O_3 in clean, maritime air, e.g. Kley et al. (1996); Pan et al. (2015)) and long-range transport processes to this region ("high" O_3 from polluted or stratospheric origin, e.g. Anderson et al. (2016); Randel et al. (2016); Tao et al. (2018)). (2) The abundance of ozone is important since the hydroxyl (OH) radical essentially defines the oxidizing capacity of the local troposphere. The close coupling of O_3 and OH in the very low NO_x environment of the TWP (Levy, 1971) allows estimation of the OH abundance from O_3 and relative humidity (RH) measurements and thus an assessment of chemical lifetimes (e.g., Rex et al., 2014; Nicely et al., 2016; Bozem et al., 2017).

Major research activities focusing on tropospheric air chemistry and O_3 observations have been conducted in the wider region since the late 1980s (e.g., Pan et al., 2017 and overview in Müller, 2020). The typical tropospheric composition of the TWP has been related to the local humid, marine, and pollutant-free environment, favouring O_3 destruction (e.g., Kley et al., 1996; Levy, 1971):

$$O_3 + h\nu \quad \rightarrow \quad O_2 + O(^1D) \qquad (\nu < 310\,\text{nm}) \tag{R1}$$

$$O(^1D) + H_2O \quad \rightarrow \quad OH + OH \tag{R2}$$

Observations in the TWP found low NO_x concentrations inhibiting O_3 production and thus facilitating an O_3 loss rate via the above reactions of 3.4% per day for the tropospheric column (Crawford et al., 1997). For boundary layer O_3 in the equatorial Pacific the efficiency of this loss mechanism results in a lifetime of around five days (e.g., Liu et al., 1983; Kley et al., 1997). Deep convective outflow and overturning processes lift the clean boundary layer air to the Tropical Tropopause Layer (TTL). In conjunction with a lack of in situ net O_3 production this creates a well-mixed, humid tropospheric profile with a uniform vertical O_3 distribution (e.g., Pan et al., 2015). These typical dynamical conditions are conducive to a respective zonal wave one pattern with a persistent tropospheric O_3 minimum in the TWP in particular (e.g., Thompson et al., 2003b; Rex et al., 2014).

Many studies highlight dry intrusions of enhanced O_3 volume mixing ratios (VMR) against the humid, ozone-poor background as characteristic features of the mid-troposphere for the wider tropical Pacific (e.g., Newell et al., 1999; Stoller et al., 1999; Thouret et al., 2000; Browell et al., 2001; Oltmans et al., 2001; Hayashi et al., 2008; Pan et al., 2015; Anderson et al., 2016). The importance of these distinct, anomalous layers for local air composition and climate forcing are often acknowledged (e.g., Mapes and Zuidema, 1996; Kley et al., 1997; Yoneyama and Parsons, 1999). Their genesis, source region and impact on the local radiative budget and oxidizing capacity are, however, the subject of an ongoing debate (Anderson et al., 2016; Randel et al., 2016; Nicely et al., 2016; Tao et al., 2018). Most studies agree, that they have been advected from remote regions and thus indicate a departure from dominating local conditions, i.e. an absence of the local imprint on air composition (see Anderson et al., 2016, for an overview).

A long-term monitoring of tropospheric O_3 in the TWP as a key region of stratospheric entry has yet been missing (Smit and Thompson, 2021), but is essential to clarify the source regions of air masses and their annual and interannual variability. All relevant major research campaigns in the TWP were temporarily limited to specific seasons and years (e.g. PEM Tropics/West

(Newell et al., 1996), CEPEX (Kley et al., 1996), TransBrom (Krüger and Quack, 2013; Rex et al., 2014), CONTRAST/CAST (Pan et al., 2017; Harris et al., 2017)). To fill the observational gap, the Palau Atmospheric Observatory (PAO) has been established in 2015 and has since been providing an unprecedented regular balloon sounding program for O_3 and RH. It is
60 located in the center of the warm pool on the island state Palau, 1000 km east of the Philippines (7.34° N, 134.47° E). The instrumental setup and meteorological conditions for the time series used in this study are introduced in more detail in a companion study by Müller et al. (2024) (cf. Müller, 2020).

   The aim of this study was to examine major air mass transport processes and pathways to the TWP troposphere by using balloon-borne O_3 and RH measurements from the PAO. Based on our process understanding explained in Section 3.1.3, we
65 propose five major air mass pathways to Palau resulting in distinct relations between the O_3 abundance and RH in the column of air above the TWP. The continuous 4 years ozone- and radiosondes time series (2016-2019) enables a seasonal analysis of the source regions, reflected mainly in the O_3 variability. We distinguished between air mass categories first using a statistical, data-based approach and performed a seasonal analysis. Lagrangian backward trajectories were then used to examine according differences in air mass origin. A potential vorticity (PV) analysis was included to investigate a possible stratospheric origin.

70   In the following, we first introduce the observational data (Sect. 2) and methods (Sect. 3) used to define different categories of air masses, which we relate to different pathways to Palau (Sect. 3.1.1). Main results of this study are the characterization of seasonal tropospheric air mass variability (Sect. 4.1) and the verification of our process-based understanding of air mass transport using trajectory modelling (Sect. 4.2). After a discussion (Sect. 5), we conclude (Sect. 6) that the maximum of the mid-tropospheric seasonal O_3 cycle can be associated with long-range transport mainly from potentially polluted areas in
75 South East Asia. We found no evidence of transport from the extra-tropical stratosphere. Additional figures with more details on the full seasonal extent are in the Appendix.

2 Data

2.1 Sondes

Our analysis is based on Electrochemical Concentration Cell (ECC) ozonesonde and radiosonde observations from 01/2016-
80 10/2019 conducted at the PAO. Balloon-borne measurements with ECC ozonesondes (Komhyr, 1969; Smit, 2014) are the most practical way to observe and continuously monitor O_3 in situ, especially at more remote sites (e.g., Thompson et al., 2019). The specific instrumentation (models SPC 6A and Vaisala RS92/41) and dataset are introduced and described in detail by Müller et al. (2024), who provide additional meteorological and climatological context for the Palau time series. While carefully following the Standard Operating Procedures (SOP) as recommended by Smit (2014), the O_3 VMR are calculated using a
85 pressure dependent background current correction (see Müller et al., 2024, for details). Figure 1 shows a time-height cross-section of the dataset with individual soundings marked by arrows, ozone in color-filled contours and RH observations below 30 % enclosed in hatched contours. Fortnightly measurements, mostly during mid-day, are complemented by one or two intensive campaigns per year. The onset of measurements in the beginning of 2016 coincides with a very strong El Niño event (e.g., Huang et al., 2016; Diallo et al., 2018). As a consequence and in compliance with acknowledged El Niño Southern Oscillation
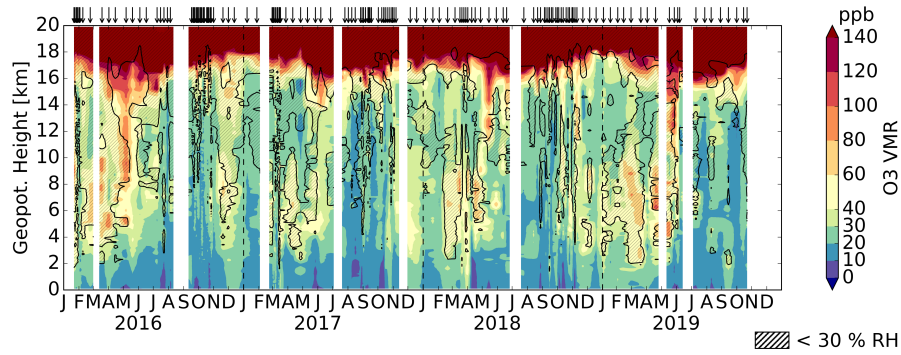
Figure 1. Tropospheric (0–20 km) time-height cross-section of O_3 VMR (in color-filled contours) and coinciding RH observations below 30 % (hatched areas enclosed in black contours) derived from PAO sounding data; arrows on top indicate individual soundings; data is linearly interpolated between soundings; measurement gaps longer than 20 days are in white, beginning 7 days after/before the last/next sounding; note the non-linear scaling; O_3 VMR are calculated using a pressure dependent background current correction, see Müller et al. (2024) for more details.

(ENSO) indices (cf. Müller et al., 2024), data before August 2016 was disregarded in some of the following statistical seasonal analysis and will be referred to as "excluding El Niño 2016". The 2019 El Niño episode, weaker in nature, is still included.

The sparsity of the O_3 data with a sounding frequency of zero to eleven launches per month and the resulting non-uniform distribution of the data affects the assessment of the temporal variability in our 4-year time series, which is still short for climatological studies. Details about our statistical averaging calculations can be found in the Appendix B. For the trajectory analysis, the dataset was limited to 138 soundings due to missing meta data (timestamps) in some of the soundings and the vertical profile resolution was reduced by selecting every 10th sonde reading. This dataset will be referred to as the trajectory dataset, including 13627 individual observations in the 5–10 km altitude range.

2.2 Meteorological Data

Back trajectory calculations were driven by 3D meteorological fields and diabatic heating rates from the European Centre for Medium-Range Weather Forecasts (ECMWF) Reanalysis data ERA5 (Hersbach et al., 2020) retrieved in a 1.125° x 1.125° horizontal and 3 h temporal resolution. ERA5 uses a parameterization for convection on the subgrid-scale. Isolated deep convection is not captured, but the net wind flow from each grid cell is zero (Hersbach et al., 2020). While our trajectory model does not calculate convective transport, the ERA5 input therefore implicitly allows us to capture synoptic-scale convective processes.

3 Methods and Analysis

The identification of differences in air mass origin by local O_3 and RH profile measurements naturally depends on the air mass definition itself. We chose air mass categories derived from statistical analysis of the two tracers, O_3 and RH, from the PAO

balloon-borne time series, which reflect our process understanding in this particular location. The chemical composition of the tropospheric column above Palau is governed by the interplay of local and non-local atmospheric processes in time and space. Our air mass categories represent these differences in chemical or dynamical properties and allow attribution to local or non-local source regions. The tropospheric column of a single day can consist of a variety of air masses, sometimes visible as distinct layers within the tracer profiles.

In the following, we use $O_3\pm RH\pm$ as a qualitative notation for air masses of low ("-") or high ("+") O_3 or RH respectively (compare e.g. Stoller et al., 1999). This leads to four qualitative categories, which we use to explain our process understanding and for comparison with previous studies (Sect. 3.1.1). The "Δ" symbol denotes quantitative air mass categories by anomalies (positive, "+" or negative, "-") from atmospheric background profiles (i.e. close to zero anomalies, denoted as "○") as defined by our statistical approach. Within this anomaly space, we established a quantitative grid with nine categories with boundaries derived from the distributions of O_3 and RH anomalies, ΔO_3 and ΔRH (Sect. 4.1.3). With this approach, we particularly targeted the questions of local or non-local genesis of background air masses ($\Delta O_3 \circ \Delta RH \circ$), which are humid and ozone-poor, and anomalously dry O_3-rich air ($\Delta O_3 + \Delta RH$-) together with their respective seasonality.

3.1 Air Mass Definition

3.1.1 Tracers and Process Understanding

O_3 is a common tracer in transport studies within the TWP, with typical dynamical conditions being conducive to a tropospheric column of low O_3 VMR attributed to local air masses (e.g., Kley et al., 1996; Pan et al., 2015). Dominant marine convection leads to low NO_x concentrations and subsequently low O_3 production rates (e.g., Crawford et al., 1997; Rex et al., 2014). In this environment the HO_x driven loss of O_3 is favored (see reaction R2) resulting in a lifetime of about five days for boundary layer O_3 (e.g., Liu et al., 1983; Kley et al., 1997). The low NO_x environment is fostered by dominating easterly winds in the annual mean and most of the troposphere (Müller et al., 2024). Most of the air reaching Palau has crossed the Pacific and has thus been cleaned of O_3 precursors from anthropogenic or other continental pollution. Palau has a hot, humid and wet climate all year, resulting in a continuously high convective activity (Gettelman and Forster, 2002; Müller et al., 2024). This persistent high convective activity creates a well-mixed profile of uniformly low O_3 VMR throughout the free troposphere, as illustrated in Fig. 2a. We refer to this as the clean state of the atmosphere or simply "background".

Layered structures of higher O_3 VMR in the mid-troposphere disturbing the uniform low O_3 profile are often observed and a signature of non-local air masses (e.g., Pan et al., 2015; Anderson et al., 2016; Randel et al., 2016). Figure 2b shows an example profile with two distinct layers of enhanced O_3 levels (> 50 ppb) around 4 and 8 km, interrupting otherwise quite constant levels of low O_3 VMR (~ 25 ppb). Enhanced tropospheric O_3 levels are generated either by photo-chemical processes in high tropospheric NO_x regimes, i.e. in polluted air masses, or by photo-dissociation of O_2 in the stratosphere and subsequent transport to the troposphere. In situ net O_3 production is unlikely at this altitude in the remote TWP, which is far from pollution sources and shows a lack of lightning activity (Christian, 2003; Cecil et al., 2014). Free tropospheric O_3 life times are in the order of weeks and comparable to the dynamical timescales of long-range transport within the tropics and from the subtropics
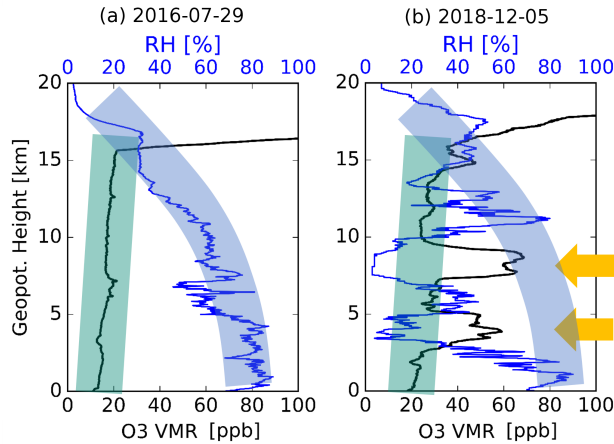
Figure 2. Example tropospheric O_3 VMR (black lines) and RH (blue lines) profiles from the PAO for the background atmosphere (a) and anomalously dry ozone-rich layers (b). The ideal shape for the background atmosphere in (a) is illustrated in green and blue shading; two layers disrupting the respective background are indicated by yellow arrows in (b).

140 (e.g., Folkins, 2002; Ploeger et al., 2011). Thus, air masses transported either from polluted areas elsewhere or the extra-tropical stratosphere can retain their high O_3 VMR until arrival in the deep tropics.

To complement O_3 as an indicator of air mass origin, we made use of RH as a measure of vertical displacement of air masses. The benefit of using RH is the readily available data from the combined sonde measurements. The dominant anti-correlation between O_3 and RH in the PAO dataset further suggests closer examination of RH (Figs. 1 and 2). RH allows us to distinguish
145 between different underlying processes affecting either local or non-local air masses (e.g., Hayashi et al., 2008; Schoeberl et al., 2015). Local air masses of low O_3 VMR often show high RH values (O_3-RH+) in accordance with the assumed dominance of convective activity and uplift. The example in Fig. 2a shows, that RH values characteristically decrease with altitude, but remain greater than 45% throughout the mid-troposphere (cf. Mapes, 2001). Non-local, ozone-rich air masses often correspond to low RH compared to the air masses above and below the humid tropical column (O_3+RH-). The depressed RH levels can
150 be explained by either stratospheric origin or various dynamical processes during transport, mostly involving a descent of air masses towards Palau which results in adiabatic compression and heating of the air, reducing RH at constant absolute humidity (Cau et al., 2007; Dessler and Minschwaner, 2007; Anderson et al., 2016). The study of RH data thus supports our understanding of processes governing O_3 variability above Palau.

The competing hypotheses for the genesis and origin of O_3+RH- air demand the use of an additional tracer (e.g. Stoller
155 et al., 1999). In this study, we use potential vorticity (PV) as a dynamical tracer to identify a potential stratospheric origin of air masses. We assume a significant in-mixing of extra-tropical stratospheric air for air masses with an absolute PV greater than 1.5 PVU for at least one day during ten days before arrival in Palau (Waugh and Polvani, 2000; Kunz et al., 2011).

In conclusion, we propose four qualitative categories of air masses and five different pathways identifiable by our tracers, as illustrated in Fig. 3. Ozone-depleted air masses (O_3-, turquoise colors) are of local or Pacific, convective origin and ozone-
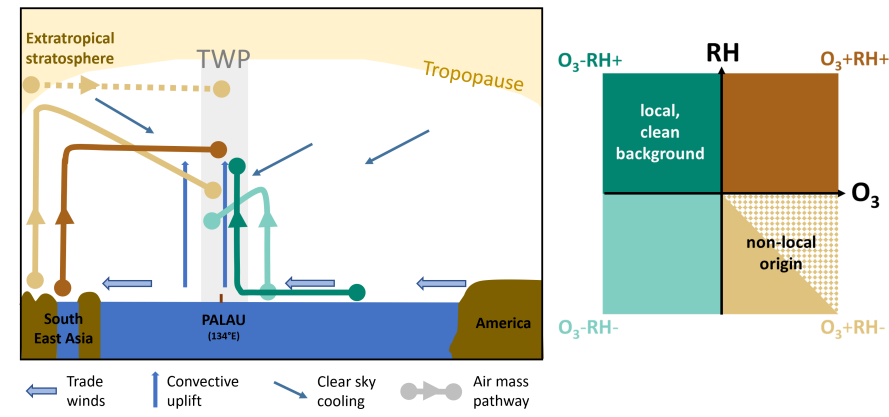
Figure 3. Schematic for transport pathways to Palau and the TWP on the zonal plane; major dynamical drivers are marked with arrows (blue colors), transport pathways are color-coded according to the air masses' O_3/RH characteristics shown in the qualitative grid (turquoise colors for O_3-, brown colors for O_3+, hue for RH±); O_3+RH- air (light brown) masses above Palau may have followed two of the five shown pathways, indicated by a solid and dotted line in the schematic (for details see text).

160   rich air masses (O_3+, brown colors) originate from non-local pollution or the stratosphere. High RH results from a dominant convective uplift of air masses (RH+, darker hues), while low RH indicates a stratospheric origin or dehydration of previously lifted air masses during transport due to clear sky cooling and descent (RH-, lighter hues). O_3+RH- air is characteristic for two different pathways (solid and dotted light brown lines in Fig. 3), thus representing two different types of air masses.

As discussed above, the two important air mass categories are tied to the dominant anti-correlation of O_3 and RH above
165   Palau: O_3-RH+ background air and O_3+RH- air masses occurring mostly in layers interrupting the background. Air masses with positively correlated O_3 and RH are observed less often and more difficult to assess. O_3+RH+ air masses (dark brown) are potentially caused by non-local pollution convectively lifted in the source region and transported rapidly towards Palau on the same altitude, conserving the high humidity. We further suggest, that O_3-RH- air (light turquoise) consists of clean boundary layer air convectively lifted in the Pacific vicinity of Palau, dehydrated due to clear sky cooling during transport.
170   Other processes, like remoistening or in-mixing of mid-latitude air during transit to the TWP could also play a role (Cau et al., 2007; Sherwood et al., 2010; Schoeberl et al., 2015; Tao et al., 2018) and are difficult to assess just using the tracer data.

3.1.2   Previous Approaches

To detect and assess anomalous layers from balloon and aircraft profiles different methods have been applied (Stoller et al., 1999; Thouret et al., 2000; Hayashi et al., 2008; Pan et al., 2015). Stoller et al. (1999) used data from three NASA campaigns
175   (PEM-Tropics, PEM West A and B) to calculate a free tropospheric background mode for various atmospheric constituents (O_3, H_2O, CO, CH_4) and for individual profiles. Using a spike detection approach, they produced extensive statistics for the frequency of anomalous layers in the whole tropical Pacific region for two different seasons. The same methodology was

applied to MOZAIC aircraft data by Thouret et al. (2000). Its main disadvantage lies within an arbitrary threshold used to determine the background mode. Despite the statistical uncertainty, Stoller et al. (1999) recognized the importance of anomalous layers in tropical Pacific profiles and emphasized their role in atmospheric chemistry modeling due to their frequent occurrence.

A similar analysis of longer time series from three SHADOZ sites (Southern Hemispheric Additional Ozonesondes Network Thompson et al., 2003a, b, 2012, 2017) confirms the frequent occurrence of dry enhanced O_3 layers below 12 km (Hayashi et al., 2008). Using a statistical method for the layer detection, the study found respective layers in approximately 50 % of profiles per year and station with differing seasonal variations. The study relies on the separation of a wet and distinct dry season at the respective stations, which is not applicable for the Palau site (cf. Müller et al., 2024).

Pan et al. (2015) isolated the low O_3 background or "primary mode" by removing all "dry" data with RH less than 45 % for all observations during the CONTRAST campaign (Pan et al., 2017). They thus refrained from resolving the individual vertical structure of layers, but proposed the RH threshold as an overall criterion in the free troposphere to separate local and non-local air masses. Pan et al. (2015) emphasized the possible variability of air mass origin within the individual vertical column, which is obscured in seasonal or even annual profile averages, i.e. layered structures in the O_3 profile hidden within the typical so-called "S"-shape (cf. Sect. 4.1). Their method, however, seems limited to the specific sites and season of the CONTRAST campaign, as it does not yield a robust output for the Palau data during all seasons (Müller et al., 2024).

3.1.3 Statistical Definition of Background and Anomalies

For a quantitative definition of air masses above Palau, we first determined background profiles in the free troposphere from the PAO O_3 and RH time series. These profiles represent humid, ozone-poor, local air masses that are controlled by convective influence and not by long-range transport. This was performed on a statistical and monthly basis and aimed to identify profile shapes similar to the signature profiles in Fig. 2a. For the monthly O_3 VMR background profiles we chose the 20th quantile (Q20) profiles. Q20 guarantees sufficiently low O_3 values to avoid a "belly" shape of the profiles, typical for tropical average O_3 profiles. For the monthly RH background profiles we chose the 83.3th quantile (Q83) profiles. Q83 is the upper boundary of the central 66.6 % range, guaranteeing high humidity. Fig. 4 shows an example of these background profiles for March. The monthly quantile profiles have been vertically smoothed using first a 1-km-binning and then exponentially weighted moving averages with altitude (see also Figs. A3 and A4). Fig. 4 includes the median and central 66.6 % ranges for both tracers separately and is calculated from 16 individual profiles (see Müller, 2020, for more details).

Our method roughly followed the approach of Hayashi et al. (2008). However, Hayashi et al. defined air masses above the 83.3th quantile as O_3 enhanced layers. With the Q20 limit for O_3 we used a less conservative approach, because the Palau background atmosphere is characterized as a uniform, well-mixed low O_3 profile, caused by uplift of ozone-poor boundary layer air in active convection. We chose this particular O_3 quantile to yield the most uniform, "straight-line" profile in the free troposphere for all monthly averages of the given time series. This essentially smoothes out any interrupting layers occurring at varying altitudes in individual profiles. While Hayashi et al. analyzed RH in ozone-enhanced anomalous layers in contrast to the air masses above and below, we applied the statistical approach to both tracers and chose Q83 for RH to detect typical convection associated with the background. The resemblance of both the particular low O_3 and high RH quantiles with the
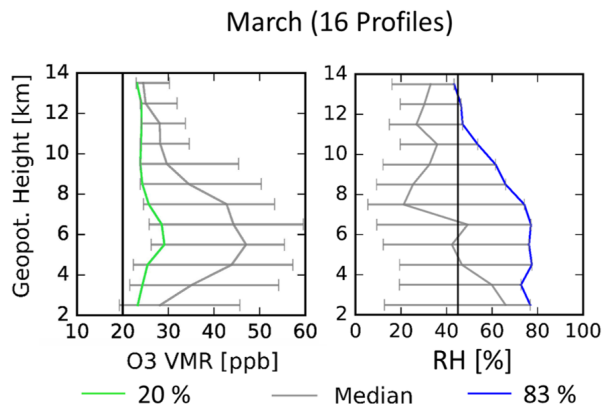
Figure 4. O_3 VMR and RH statistics for the month of March as example for Palau free tropospheric profiles as a function of altitude: the 20th quantile (Q20) for O_3 is shown in green and the 83.3th quantile (Q83) for RH in blue (both vertically smoothed using exponentially weighted moving averages); the median is marked in grey and the central 66.6 % range in grey horizontal bars; number of included individual profiles in brackets, for orientation 20 ppb O_3 VMR and 45 % RH are marked in black (see also Figs. A3 and A4).

example of an individual background profile in Fig. 2a is evident. The monthly averaging accounts for the seasonal variability of the background as the uniform O_3 profile shifts towards higher base VMR from summer/fall to winter/spring (compare Figs. 2 and A3).

215   In a second step, we determined the anomalies against the monthly background profiles, denoted in the following by ΔO_3 and ΔRH. These are calculated for individual measured O_3/RH pairs within each sounding and in their respective month-altitude bin. Within the anomaly space, we define a new background air mass category, "$\Delta O_3 \circ \Delta RH \circ$", with close to zero anomalies in both tracers. We further denote eight other quantitative air mass categories with combinations of positive ("+"), negative ("-") or close to zero ("$\circ$") anomalies for both ΔO_3 and ΔRH individually (Sect. 4.1.3). In this study however, we

220 limited further analyses to the two most interesting quantitative air mass categories, $\Delta O_3 \circ \Delta RH \circ$ and $\Delta O_3 + \Delta RH-$, i.e. per definition humid, ozone-poor background air masses and anomalously dry, ozone-rich air masses. In contrast to Hayashi et al. we did not assess the vertical structure of the anomalous layers in individual profiles. Hence, neither the layer thickness nor the layer position within the profile were considered. Any measured data point of a profile was quantitatively attributed to one of nine air mass categories, which were then analyzed "in bulk". In our following analysis, we further focused on the altitude

225 region between 5 and 10 km, where the weakest cloud-mass divergence occurs, i.e. the weakest convective detrainment (Folkins and Martin, 2005) and the greatest frequency of anomalous layers.

3.2 Trajectory Analysis

We deployed the trajectory module of the fully Lagrangian chemistry and transport model ATLAS (Wohltmann and Rex, 2009; Wohltmann et al., 2010) driven by ERA5 data (see Sect. 2). The model uses a hybrid vertical coordinate, which gradually

230   transforms from pressure at the surface to potential temperature in the stratosphere. The corresponding vertical velocities change from vertical winds in pressure coordinates to diabatic heating rates, respectively.

    10-days backward trajectories with a time step of ten minutes were initialized at the location and time of every tenth sonde reading of a profile (approximately every 50 m, i.e. 20 trajectories per km) for all profiles within the trajectory dataset. They are considered as a footprint for transport pathways towards Palau. We assume O_3 to be a passive tracer during transport, i.e.
235   did not implement chemical reactions. This assumption is justified for dry, mid- to upper tropospheric air because of photochemical lifetimes of O_3 in the order of several weeks to months under these conditions. In the wet lower troposphere and marine boundary layer this approach is only valid for a few days, because of O_3 lifetimes in the order of days (e.g., Thompson et al., 1997). Convection is not treated explicitly in the model setup, but partly reflected in the reanalysis data. Anderson et al. (2016) found air parcel ages of around 10 days in the TWP in winter 2014, when stopping their trajectories at the point of last
240   precipitating convection based on satellite observations of cloud top height and precipitation. We therefore assume no "reset" of the composition of our air mass within five days and stop our trajectories five days before arrival to identify the origin.

4   Results

We first present the variability of the PAO tropospheric O_3 time series to assess air mass seasonality and the application of our method to determine different groups of air masses. Then, our results from the trajectory analysis are shown, first investigating
245   general seasonal tracer variability, and second combining these results with our method to identify different air masses (Fig. 3). A physical interpretation of the results follows in the discussion (Sect. 5).

4.1   Air Mass Variability

4.1.1   Annual O_3 Variability

Figure 5 shows time-height cross-sections of the annual variability of tropospheric O_3. Figure 5 (a) shows monthly means, (b)
250   anomalies from the annual mean profile and (c) the annual mean profile of the overall time series (black solid line), excluding El Niño 2016. Panel (c) also shows the standard deviation (SD) and the relative standard deviation (RSD) of the overall annual mean profile (dashed and dotted lines, respectively), as well as the annual mean profiles of individual years (colored lines). As the fraction of the SD relative to the annual mean, the RSD can be considered as a measure of variability with altitude (cf. Ogino et al., 2013). The annual mean tropospheric O_3 VMR profile (Fig. 5c) has an "S"-shape typical for tropical sounding
255   stations (e.g., Folkins, 2002; Thompson et al., 2003a, b; Pan et al., 2015). O_3 VMR are lowest in the boundary layer (< 20 ppb) and also low between 10 and 12 km (< 30 ppb). They increase in the mid-troposphere to about 35 ppb and again above 12 km towards their stratospheric maximum, which is an order of magnitude higher. The interannual variability of the annual mean O_3 profile is low for all years with the exception of 2016.

    The monthly O_3 VMR (Figs. 5a and b) reveal two dominant signals: an annual cycle in the 5–10 km altitude range with
260   the maximum from February until April (30–60 ppb) 2–3 times greater than the minimum from July until October (10–30
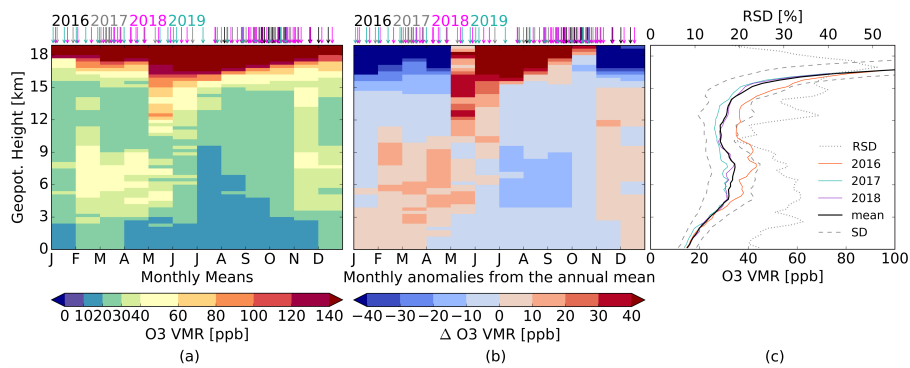
Figure 5. Monthly means (a), anomalies from the annual mean (b) and the annual mean profiles (c) for individual years (thin colored lines) and for the whole time series excluding El Niño 2016 (thick black line) with standard deviation for the whole time series (grey dashed lines) and relative standard deviation (RSD) (grey dotted line); individual soundings are marked as arrows above with different colors for different years; non-linear scaling is used in (a) to match the different orders of magnitude in the lower and upper troposphere (compare Müller et al., 2024, Fig. 6)

ppb), and a reverse, strong cycle in the TTL with maximum anomalies (> 40 ppb) from June until September. The peak in RSD of 50 % at about 17 km reflects the strong TTL cycle. The enhanced variability in mid-tropospheric O_3 (RSD ~ 30 %) corresponds with the cycle revealed by the monthly means. Annual variations in O_3 observations are smallest between 10-12 km and especially in the boundary layer (RSD ~ 20 %), thus coincidental with the O_3 minima of the annual profile. The

265   regionally typical ozone-poor background is clearly subject to seasonal variations.

4.1.2 Seasonal O_3 Profiles

A more detailed analysis of the seasonal O_3 variability helps to identify recurring seasonal characteristics and differences in controlling processes like synoptic or meteorological conditions. Therefore, we divided our time series into four seasons, shifted by one month compared to the temperate climate seasons: November-December-January (NDJ), February-March-April (FMA),

270   May-June-July (MJJ) and August-September-October (ASO). These Palau seasons reflect different influences dependent on the time of the year and were chosen empirically by sorting monthly O_3 profiles (Müller et al., 2024, Fig. A1) by similar shape, considering the full free-troposphere. The resulting four most different types of profile shapes are shown in Fig. 6. The Palau seasons turned out to be centered around the equinoxes, which is reasonable for a tropical station.

In the 5–10 km altitude range FMA and ASO show the largest differences and represent the extremes of the mid-tropospheric

275   cycle. The "S"-shape of the annual mean profile prevails in the winter seasons, i.e. in NDJ and most pronounced in FMA. The interannual variability is particularly high during FMA from 5 to 10 km with generally enhanced O_3 VMR between 40 and 50 ppb (Fig. A1). The ASO profile is closest to the uniform background profile (20–25 ppb O_3 VMR) with little interannual variability, while having the highest sampling rate (59 profiles). We thus refer to ASO as the background season. In the TTL, both extreme seasons, ASO and FMA, show a pronounced O_3 minimum, except during the 2016 El Niño FMA season (Fig.
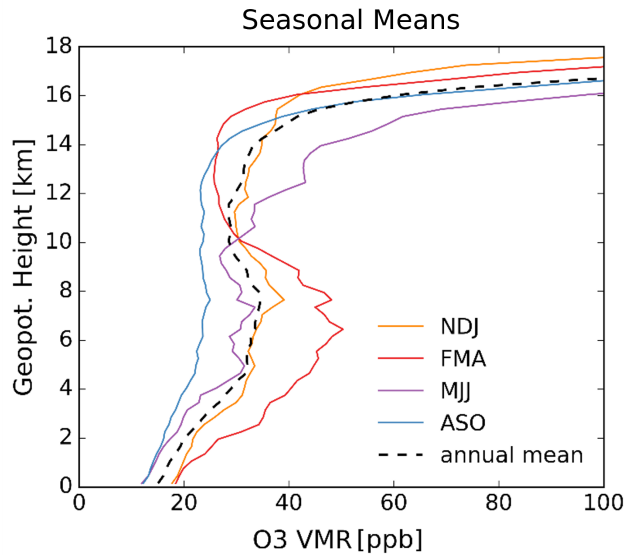
Figure 6. Seasonal mean O$_3$ VMR profiles (colored solid lines) in comparison to the annual mean (dashed black line), all excluding El Niño 2016, for Palau seasons November-December-January (NDJ), February-March-April (FMA), May-June-July (MJJ) and August-September-October (ASO).

A1). The steep onset of higher levels of (stratospheric) O$_3$ VMR in ASO occurs at lower altitudes compared to the NDJ and FMA seasons.

MJJ and NDJ can be considered as intermediate seasons with respect to the mid-tropospheric cycle, i.e. O$_3$ values here are in between the minimum and maximum. The NDJ profile resembles the annual mean profile up to about 14 km, while the MJJ profile diverges from the annual mean above 10 km towards higher values. The resulting tilted line shape during MJJ, compared to the straight line profile during ASO, implies a more gradual increase of O$_3$ in the UTLS (cf. Müller et al., 2024) and a lack of a pronounced O$_3$ minimum in the UT. In MJJ, the tropopause is at its lowest altitude of the year, thus is the occurrence of high levels of stratospheric O$_3$ VMR.

4.1.3 O$_3$ and RH: Background and Anomalies

The application of our method to separate air masses on the full PAO time series for the free troposphere (3–14 km) yields the distribution of anomalies from the background profiles, ΔRH and ΔO$_3$, given in Fig. 7 (see also Sect. 3.1.3). The 2D-histogram in Fig. 7a shows ΔO$_3$ versus ΔRH from all months and altitudes as percentages of the total count of all measured free-tropospheric O$_3$/RH data pairs in grey-scale. Data along the zero lines within this anomaly space indicate zero anomalies and thus an attribution to the respective background profiles, Q20 of monthly O$_3$ VMR and Q83 of monthly RH values. The marginal 1D-histograms show the distributions of both tracers individually normalized to unity.

Both ΔRH and ΔO$_3$ show heavily skewed distributions, with a long tail in the ΔO$_3$ distribution towards less frequent high O$_3$ occurrences and even a bimodal distribution for ΔRH with a secondary maximum in the tail towards dry air masses. These distributions motivate the separation of air masses into three domains for both parameters, one corresponding to the low tail, one to the bulk of the observations and one corresponding to the high tail. Overall this leads to nine quantitative air mass categories in a three times three grid referred to as the quantitative grid (Fig. 7b). The boundaries were chosen empirically with respect to the shape of the distributions with a range of -5/+15 ppb ΔO$_3$VMR and -20/+5 % for ΔRH for the central group.

In particular, the correlated occurrence of air masses with high O$_3$ and low RH (ΔO$_3$+ΔRH-) stands out as a low, but separate population in Fig. 7a (lower right quadrant), while the central group (ΔO$_3$○ΔRH○) represents the most frequent conditions and is referred to as background category (not to be confused with the background profile), since anomalies from the background profiles are smallest. In this study, we focus on the distinct population of ΔO$_3$+ΔRH- air masses in contrast to this background category. ΔO$_3$○ΔRH○ air masses are characterized by significantly higher RH and lower O$_3$ and are therefore also referred to simply as the humid, ozone-poor background.

The anomalies are mostly clustered within 20 ppb along the ΔO$_3$ zero line indicating an overall dominance of ozone-poor air masses. Apart from the tail towards less frequent higher ΔO$_3$, the narrow distribution is nearly Gaussian and centered around 0 ppb ΔO$_3$ VMR with a tendency towards positive values. The majority of ΔRH values appears between -60 and 20 %. The bimodality of the ΔRH distribution is persistent in all seasons with the exception of MJJ (Fig. A5). The primary, dominant mode is centered slightly off the ΔRH zero line towards negative values, i.e. the majority of measured RH values matches the Q83 or slightly lower values of the respective month-altitude bin. The secondary mode occurs for $Delta$RH values 40 % lower than their background profiles estimates.

Figure 8 shows the ΔO$_3$/ΔRH distribution for the seasons FMA and ASO. As expected from the previous analysis, ΔO$_3$+ΔRH- are almost absent in ASO (Fig. 8a), emphasizing that the season represents an overall ozone-poor, mostly humid background in the free troposphere. In contrast to the seasonal mean FMA O$_3$ profile with elevated O$_3$ levels in the mid-troposphere (Fig. 6), the FMA anomalies distribution (Fig. 8b) reveals a dominance of background category air masses over ΔO$_3$+ΔRH- air masses within the free troposphere. A statistical view on the seasonal occurrence of different air masses in the mid-troposphere emphasizes the year-round dominance of ΔO$_3$○ΔRH○ air, which were observed in more than 70 % of profiles within each season (Fig. A6).

4.2 Air Mass Transport and Processes

4.2.1 Trajectory Origin by Season

In the following, we focus on the 5–10 km altitude range with the most frequent occurrence of ΔO$_3$+ΔRH- air masses and the largest seasonal differences in O$_3$ VMR (cf. Fig. 6 and Sect. 3.1.3). A footprint of air mass transport to Palau is analyzed using 10-days backward trajectories for the study period (2016–2019) sorted by season arriving in Palau in the 5–10 km altitude range (Fig. 9). For better visualization, a representative subset was chosen, displaying only every 20th trajectory of a profile
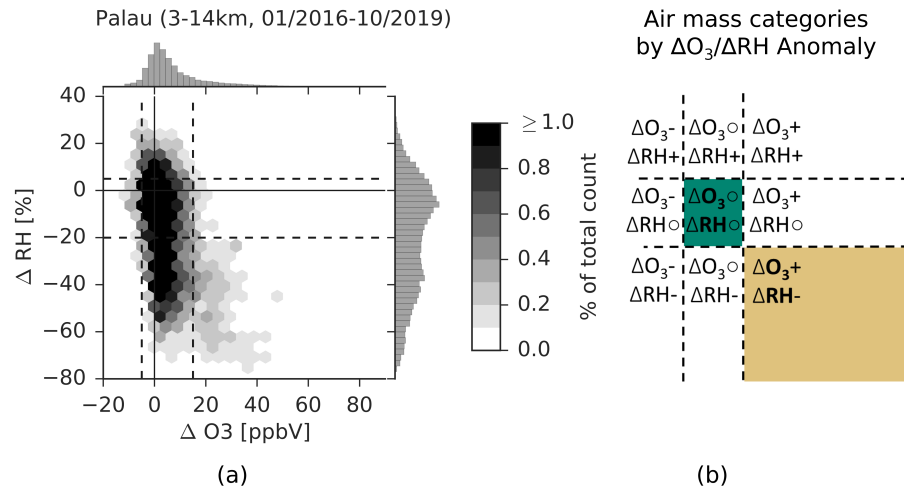
Figure 7. (a) Free-tropospheric (3–14 km) relation between tracer anomalies ΔO_3 VMR and ΔRH from monthly background profiles defined in Section 3.1; color shading indicates percentages of total count of measured O_3/RH data pairs per grid point; marginal plots for individual tracer anomaly distributions are normalized to unity; dashed lines refer to quantitative air mass categories in the three times three quantitative grid as illustrated in (b), with boundary values for the central grid box ($\Delta O_3 \circ \Delta RH \circ$) of -5/+15 ppb for ΔO_3 VMR and -20/+5 % for ΔRH; two target categories of the analysis are highlighted in color in (b), compare to Fig. 3.
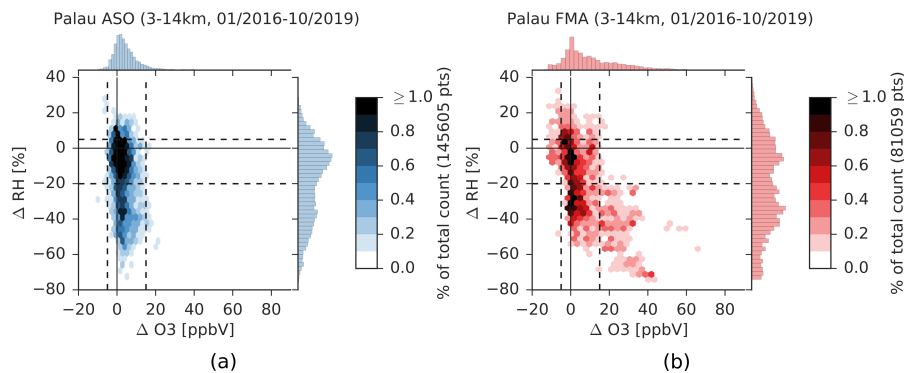
Figure 8. Seasonal free-tropospheric (3-14 km) relation between tracer anomalies ΔO_3 VMR and ΔRH, total number of datapoints in brackets, colors according to Fig. 6, more details in Fig. 7 and 6.

(roughly 1 trajectory per km). Colored line-segments show three different time periods backwards, three, five and 10 days, thus indicating the velocity of air mass transport.

Most air masses reach Palau from the east, but have traveled two different paths on different timescales. The seasonal distinction of trajectories roughly separates an Eastern Pacific pathway, dominating in MJJ and ASO, from an anticyclonic route in NDJ and FMA, connecting Palau with South East Asia and some remote areas as far as the African continent. The
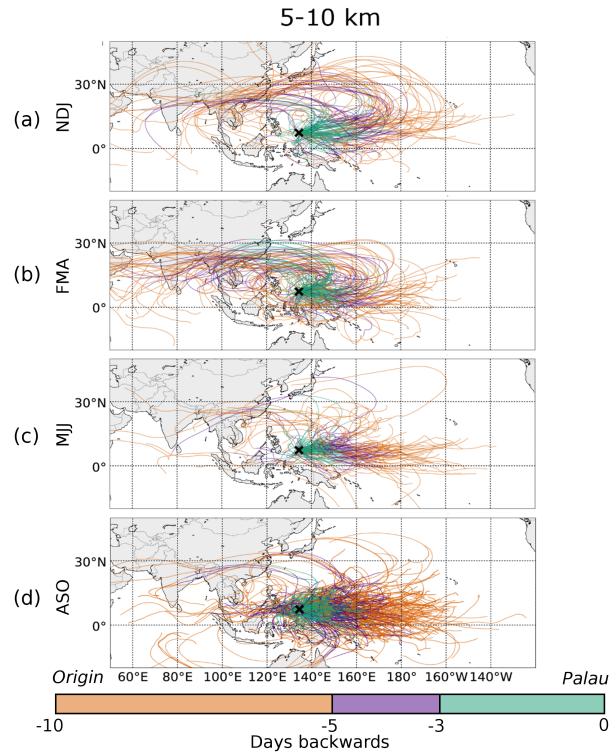
Figure 9. Geographical footprint of air masses: 10-days backward trajectories from ATLAS arriving at Palau in the 5-10 km altitude range by season (2016-2019); colored segments represent time periods of maximal three (green), five (purple) and 10 (orange) days backwards, respectively; the x marks the location of Palau; only a subset (every 20th data point of a profile, roughly one per km) of the trajectory dataset is shown, see Fig. 6 for seasons.

anticyclonic route can be associated with long-range transport on shorter timescales compared to the Pacific route. As these transport patterns are most pronounced in FMA and ASO, respectively, which also exhibit the greatest tracer differences in the mid-troposphere (compare Fig. 6), we focus on these two Palau seasons in the following.

335   The geo-spatial extent of the footprints differs significantly for season FMA and ASO. While all trajectories stay mostly within the tropical zone between 0° to 30° N, trajectories during FMA have a wider longitudinal extent than during ASO. Most ASO air masses never left the Pacific Ocean area within 10 days before arrival in Palau and have traveled shorter distances. Only a few trajectories on a Southern hemispheric cyclonic route show the influence of the Western Pacific monsoon, which is active from July to October, but governs air mass transport mostly below 5 km altitude (Müller et al., 2024).

340   Figure 10 shows the location of air masses five days before their measurement in Palau inferred from trajectories for the seasons FMA (top) and ASO (bottom) as an indication of the origin of the air masses. The geo-spatial probability density function of data points is highlighted as black contour lines in Fig. 10a. Here, the colors indicate O_3 VMR as observed upon
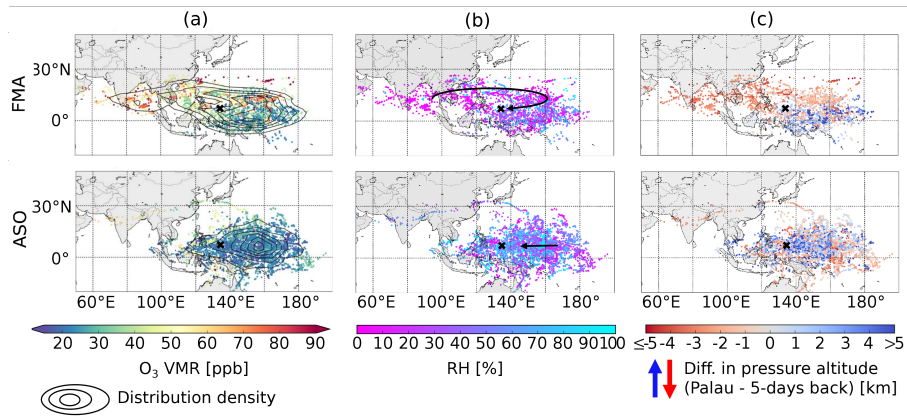
Figure 10. Origin of air masses by season: Location of air masses five days before their measurement in Palau in the 5-10 km altitude range inferred from trajectories for Palau seasons FMA (upper row) and ASO (lower row); color-coded by O_3 VMR (a), RH (b) and by difference in pressure altitude, between measurement and five days before measurement (c); black contours in (a) show distribution density and schematic arrows in (b) indicate the pathway as shown by the footprint in Fig. 9; see Fig. 6 for seasons.

arrival in Palau. Figures 10b and c show the same locations as Fig. 10a, but colored-coded by RH (b) or difference in pressure altitude (c). Red colors in panel (c) indicate descent, blue colors ascent towards Palau.

345   The dominant source region of free-tropospheric Palauan air masses, indicated by the center of the density distribution in Fig. 10 a, is located east of Palau during both seasons and corresponds to low O_3 VMR ($\leq$ 30 ppb). During FMA, this eastern center of the distribution is actually split in two parts along a latitudinal axis. The dominant part is located further south on the equator, exhibiting low O_3 VMR. The northern part of the eastern center is of higher O_3 VMR. A separate cluster of trajectory points showing enhanced O_3 VMR ($\geq$ 60 ppb) exists northwest of Palau during FMA, roughly extending from India to Taiwan.

350 As revealed by the full 10-days trajectories in Fig. 9b, all air masses of higher O_3 VMR during FMA can be related to the anticyclonic route, though some took longer than five days to travel from South East Asia to Palau. During ASO the overall unimodal distribution is centered on Palau's latitude, 20° to the East, and observations of enhanced O_3 VMR originate outside the main cluster. For both seasons, air masses with O_3 VMR greater than 60 ppb rarely originate south of Palau.

    The distinction between the two pathways is also reflected in RH (Fig. 10b) and even more clearly in the vertical displacement

355 of air masses from origin to destination (Fig. 10c). In FMA, Fig. 10c shows descended air masses originating north and ascended air south of Palau. Here, the descent of air masses corresponds with greater O_3 VMR and lower RH, although the pairwise correlation, R, of these two parameters with the pressure height difference is not strong (R=-0.53 for O_3VMR and R=0.44 for RH, for the latter cf. Fig. A7). We can, however, associate these dry, descending air masses with the anticyclonic route shown in the 10-days backward trajectory footprint.

360   For ASO air masses, the picture is not as clear, but ascent and humid air masses with low O_3 VMR are slightly dominating (Figs. 10c and A7b) and have likely followed the Pacific pathway. The pairwise correlation for pressure height difference and O_3 VMR or RH, respectively, is even lower than during FMA (R=-0.36 for O_3, R=0.35 for RH). However, there are clearly two
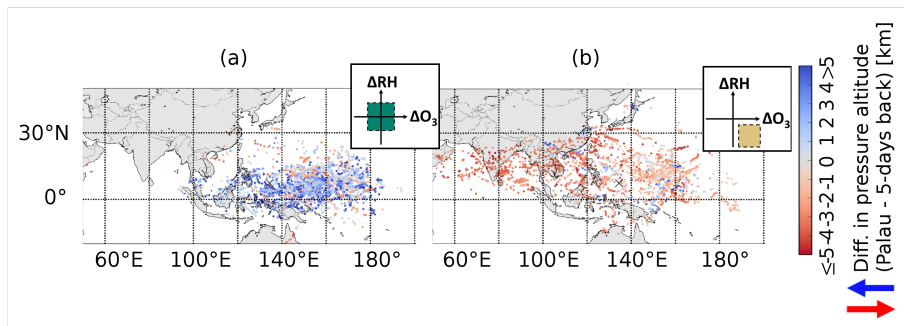
Figure 11. Origin of air masses by air mass anomalies: Location of air masses five days before their measurement in Palau in the 5–10 km altitude range inferred from trajectories for $\Delta O_3 \circ \Delta RH \circ$ (a) and $\Delta O_3 + \Delta RH$- (b) air masses, as indicated by the pictograms; color-coded by difference in pressure altitude between measurement and five days before measurement, see also Figs. 7 and 10.

main groups of air masses, one with RH below 40 %, descended mostly only 1 km, and one group with RH centered around 70 %, ascended mostly 1 km or more.

The investigation of the history of PV for Palauan air masses revealed no stratospheric pathway. Below 1 % of all 13627 trajectories stayed above 1.5 PVU for more than a day during 10 days transit to Palau. Within five days before arrival only few trajectories crossed the 1.5 PVU threshold.

4.2.2 Trajectory Origin by Air Mass

While we have looked at the origin of the trajectories as a function of season in the previous section, we now turn to the origin as a function of air mass. The classification of trajectories by quantitative air mass category as defined in Section 3.1 yields the distribution of source regions as shown in Fig. 11. Background $\Delta O_3 \circ \Delta RH \circ$ air masses originate within a compact region in the Pacific, mostly east of Palau stretching as far as 180° E. The origin pattern for $\Delta O_3 + \Delta RH$- air masses clearly show transport from the South East Asian region and along the anticyclonic path to Palau. In comparison to the seasonal analysis, the classification of trajectories by air masses shows a clear distinction for the history of vertical displacement of the air masses. On their way towards Palau most $\Delta O_3 \circ \Delta RH \circ$ air masses have been ascending, while $\Delta O_3 + \Delta RH$- air has descended.

A seasonal analysis of the trajectories sorted by air mass anomalies reveals some differences in the source regions of $\Delta O_3 + \Delta RH$- air masses (Fig. A8). The origin hot spots around India and the Southeast Asian peninsula are almost exclusively observed during FMA. The Southern Philippines and the area slightly North East of Palau are equally dominant source regions in this season. In ASO, $\Delta O_3 + \Delta RH$- air masses are less frequently observed and their origins are clustered around three main areas: 1. north east of Palau in the West Pacific, 2. between Borneo and the Southern Philippines and 3. in the New Guinea region, extending towards Northern Australia.

5   Discussion

The central goal of our study was to identify the air mass origin of TWP air and its seasonality by means of the observed O_3/RH relation above the PAO. We proposed a qualitative transport scheme for different types of air masses ($O_3 \pm RH \pm$, Fig. 3) that distinguishes between local and non-local processes. Lagrangian backward trajectories support this hypothesis. Trajectories with different air mass characteristics, defined by their O_3 and RH anomalies from statistically defined background profiles, show different geographical origins and transit properties. The PAO 4-year time series reveals the seasonality of air mass types and thus origin. Our analysis thereby confirms the usefulness of O_3 and RH as combined tracers for air mass origin in the TWP.

5.1   Seasonality and Air Mass Definition

The PAO time series provides unprecedented insight into the seasonality of tropospheric air composition in the TWP (Müller, 2020; Müller et al., 2024). An important observation from the PAO dataset is the dominant anti-correlation between O_3 and RH (Fig. 1). The annual cycles of O_3 in the mid- and upper troposphere were expected from satellite observations and previous studies, especially the zonal wave one pattern in the TTL (e.g., Thompson et al., 2003b; Randel et al., 2007), but had not been monitored continuously with in situ measurements before. The high temporal and vertical resolution of the ozonesonde dataset revealed day-to-day variations, but also the prevalence of significant seasonal signals modulating these. Especially the increased sampling frequency during the extremes of the mid-tropospheric cycle shows the robustness of this signal for Palau and the dominance of the local low O_3 mode during late summer (Fig. 6). Currently, the shortness of the time series and statistical bias due to the differences in monthly sampling frequencies have to be taken into account. A future analysis of the growing time series will be better able to assess the influence of interannual variability. The ENSO cycle will likely play the most important role in this.

The mid-tropospheric O_3 cycle is in accordance with the annual movement of the Intertropical Convergence Zone (ITCZ). The occurrence frequency of either a clean convective (local) state or a non-local state with long-range transport to the TWP is regulated by the two major barriers ITCZ and Southern Pacific Convergence Zone (SPCZ). Müller et al. (2024) showed the correspondence of the ITCZ's position north of Palau with the minimum in O_3 measurements (cf. Fig. 5). This relates to previous studies on air mass transport to the region: during the PEM-Tropics West B campaign, Browell et al. (2001) found that layers of high O_3 VMR advected to the TWP from remote polluted areas are mostly confined north of the ITCZ. Very low O_3 values were only present in the "equatorial wedge" between ITCZ and SPCZ and associated with enhanced vertical mixing in convection in the absence of gross ground pollution. Palau is enclosed between these bands during ASO (Sun et al., 2023), therefore the best season to observe the clean air background. During FMA, when the ITCZ is located furthest south, transport from higher northern latitudes is possible. MJJ and NDJ can be considered as intermediate seasons with respect to both, the mid-tropospheric cycle and the similar location of the ITCZ during its annual crossing. This feature explains, why studies related to the CONTRAST campaign which took place in January/February 2014 did not see low O_3 extremes (Pan et al., 2015; Newton et al., 2016; Nicely et al., 2016; Tao et al., 2018), and why background conditions of the region need to

be assessed by long-term measurements. Its unique location and year-round operation makes the PAO an excellent background site to study the influence of dynamics (cf. Thompson et al., 2021; Sun et al., 2023).

The strong TTL cycle as a zonal phenomenon can be mostly explained by the interplay between Brewer-Dobson and Hadley circulation (cf. Müller et al., 2024). Mass fluxes for both circulation regimes become comparable at around 16 km altitude (e.g. Folkins, 2002; Pan et al., 2014). The minimum in the vertical O_3 profile in the UT (the so called chemopause) can be attributed to deep convective outflow. Recognized as a characteristic feature of tropical profiles, low UT O_3 is often used as an indicator for deep convective detrainment (e.g., Kley et al., 1996; Folkins, 2002; Solomon et al., 2005; Gettelman et al., 2009; Paulik and Birner, 2012). Satellite observations confirm year-round convective activity in Palau, with some variability due to the traverse of the ITCZ twice a year (Gettelman and Forster, 2002; Müller et al., 2024). Müller et al. (2024) associate the occurrence of the strongest winds below 15 km when the ITCZ is furthest south or north of Palau with the poleward branch of the Hadley circulation. The low variability in UT O_3 (Fig. 5c) can hence be explained by the persistence of deep convection and the level of convective outflow in association with the Hadley and Walker circulation (e.g., Folkins, 2002; Solomon et al., 2005; Takashima et al., 2008). The months of May and June stand out in this context with higher O_3 levels between 12 and 15 km thus lacking a chemopause (Fig. 5). The dry environment at this altitude increases O_3 lifetimes and makes in situ O_3 destruction unlikely, although it is discussed as a consequence of convectively injected water vapor (Schoeberl et al., 2015; Anderson et al., 2016). The PAO dataset is predestined for future studies on the seasonality of deep convective outflow and stratosphere-troposphere exchange (STE) processes in the TTL in this region of major entry into the stratosphere in boreal winter.

The specific classification of seasons used in this study corresponds to distinct dynamical conditions. In particular, the Palau seasons can be related to the movement of the ITCZ, the main driver of dynamical variability. Our interpretation of the profile shapes is supported by the separation of trajectory footprints in Fig. 9, i.e. different dominating pathways for the different seasons, and a comparison with an analysis of SHADOZ station profiles from Java and American Samoa by Stauffer et al. (2018). They used a sophisticated clustering technique to characterize ozonesonde profile variability related to different controlling processes. Out of four cluster profiles, the low O_3 cluster associated with convective lifting of low O_3 VMR compares well with the Palau ASO profile. The cluster with highest average O_3 VMR exhibits a similar "tilted line" shape like Palau MJJ with a lower tropopause and weak gradient, explained by Stauffer et al. (2018) with STE. This corresponds well with the minimum annual tropopause height and a shift in wind regimes due to the crossing of the ITCZ around June (Müller et al., 2024). The horizontal wind is weakest throughout the entire tropospheric column in May, as the subtropical ridge shifts south with increasing altitude, which could favor quasi-horizontal transport of extra-tropical stratospheric air into the TTL. July can be seen as a transition month, as the tropopause is comparable with May and June, but mid-tropospheric O_3 VMR are as low as observed in August and September (cf. Fig. A1 in Müller et al., 2024). In July, the Western Pacific monsoon already reaches Palau in lower altitudes in the form of equatorial westerlies, but the tropopause is still low. While the construction of 3-month-seasons remains arbitrary in any case, it could be reconsidered especially for the summer months (MJJ, ASO) to further differentiate between these processes.

Our new definition of humid, ozone-poor background and anomalously dry ozone-rich air masses in relation to statistically defined background profiles allows a separation of air mass origin based on backward trajectories. Looking at anomalies, ΔO_3 and ΔRH, our method provides an improved criterion compared to using fixed thresholds based on absolute tracer values, as have been used in previous studies (e.g. Anderson et al., 2016; Nicely et al., 2016; Randel et al., 2016; Tao et al., 2018), who all defined O_3+RH- air masses with RH < 20 % and O_3 VMR > 40 ppb. Our approach using quantiles based on a 4-year time series focuses on a physically motivated background definition. A comparison between air mass categories based on absolute thresholds and our quantitative air mass categories for the PAO data set shows an improved separation of processes in the trajectory analysis, namely between ascent and descent of air masses (not shown here). The main advantage of our method compared to algorithms of layer detection in individual profiles (e.g., Stoller et al., 1999) lies within its simplicity and the consideration of the identified bimodality in the RH anomalies. In principle, it is also applicable for sounding data time series from other tropical stations. However, it may not yield the best results as atmospheric processes and mechanisms determining air composition might be specific to this geographic region.

The bimodality in RH anomalies is a striking result of our study. It further justifies our separation between $\Delta RH\circ$ and ΔRH- air masses in the quantitative grid classification (dashed lines in Figs. 7 and 8), although the exact definition of the grid boundaries could be revisited. Global probability distribution functions of RH from observations have already been shown as bimodal for different tropospheric altitudes in tropical regions, in particular within the ascending branch of the Hadley circulation (e.g., Zhang et al., 2003; Ruzmaikin et al., 2014). Our results fit into the findings of these studies. Other studies e.g. by Sherwood et al. (2006, 2010) earlier disputed the original claim of a common bimodality in RH distributions by Zhang et al. (2003). The PAO dataset now adds to this discussion. However, a comparison of the different methods arriving at RH distributions would be necessary to draw further conclusions.

A classification of free-tropospheric air mass anomalies by seasons in Fig. 8 shows the absence of ΔO_3+ΔRH- air in ASO and MJJ, as already inferred from the seasonal mean profiles (Fig. 6), compared to their prominent appearance in NDJ and FMA (see marginal 1D histograms for ΔRH in Figs. A5 and 8). During the NDJ and MJJ, both maxima in ΔRH are of similar amplitude, which emphasizes the importance of dry air masses intruding into the otherwise humid troposphere (cf. Stoller et al., 1999). While the relevance of ΔO_3+ΔRH- filaments is undisputed, other categories of air mass anomalies are encountered less often and are thus more difficult to relate to underlying atmospheric processes (cf. Sects. 1 and 3.1.1).

The selection of Q83 for RH could be revisited for the analysis of a larger time series, also in context of the ΔRH bimodality, as the maximum peak of the ΔRH distribution is mostly just below zero, i.e. background values (Figs. 7, 8 and A5). This is also reflected in the dominant occurrence of both $\Delta O_3\circ\Delta RH\circ$ and $\Delta O_3\circ\Delta RH$- found for the 5–10 km subset of the Palau data (Fig. A6). An adjustment of the RH quantile for the background profile and a corresponding shift onto the center of the $\Delta O_3\circ\Delta RH\circ$ group could still improve the air mass selection. The monthly O_3 profiles are not uniform throughout the column, which is proposed as the ideal, purely convective profile (compare Figs. 2 and A3, A4). During the months of increased occurrence of dry ozone-rich layers, i.e. FMA and NDJ, the Q20 profile still incorporates the "S"-shape, presumable caused by these layers. This effect could possibly be reduced by changing the temporal resolution from monthly to seasonal statistics, which has not

been assessed yet. A growing time series will help to validate our approach as it reduces possible biases caused by different sampling frequencies per season.

5.2 Air Mass Transport and Processes

485 The trajectories reflect the dominating general circulation patterns, namely the Hadley and Walker circulation and the trade winds, with most air masses eventually reaching Palau from the East (Fig. 9). The influence of the Western Pacific Monsoon, active from July until October, becomes most apparent below 5 km altitude (cf. Müller et al., 2024). We identified two dominating routes for air mass transport to Palau, the local, Pacific route and the anticyclonic route from Asia. On the anticyclonic route, air masses can travel from the ascending branch of the Hadley circulation towards the descending branch along the sub-

490 tropical ridge (Anderson et al., 2016). Once air parcels reach the West to Central Pacific during winter they are either diverted eastwards by the subtropical high anticyclone or are picked up by the general trade wind circulation, subsequently reaching Palau from the East. In contrast, with a subtropical ridge further north during summer, transport is governed only by the trade winds and monsoon circulation, bringing air masses from the convectively active Pacific region to Palau.

The anticyclonic flow pattern resembles the planetary wave response to tropical diabatic heating as shown for the National

495 Centers for Environmental Prediction (NCEP) reanalysis data by Dima et al. (2005). Following the theoretical concepts of Matsuno (1966), Gill (1980) and Van Tuyl (1986), Dima et al. (2005) identified a pair of upper tropospheric anticyclonic Rossby gyres located west of and at a maximum of latent heating over the western Pacific and Indian oceans. An analysis of the equatorially symmetric component of the circulation pattern reveals the year-round presence of the Rossby wave couplet at 150 hPa, located at the same longitude on the Northern and Southern hemisphere, with a seasonal shift in longitude for

500 the centers of the anticyclones from approx. 160° E in January/ February to approx. 80° E in July/ August. At Palau, the anticyclonic flow pattern is indeed dominating for back trajectories above 14 km altitude (not shown here). The equatorially symmetric nature of the Rossby wave couplet is potentially captured by some Palau back trajectories between 5 and 10 km during ASO reaching Palau from the Southern hemisphere (Fig. 9d). The lack of the anticyclonic route for midtropospheric Palau back trajectories for MJJ and ASO and the dominance of the Eastern pathway, seems to be supported by the seasonal

505 shift in longitude of the centers of the Rossby gyres in the summer months and subsequent stronger easterly flow near the equator over the western Pacific region. However, Dima et al. (2005) focused their analysis on the upper troposphere.

The results of the backward trajectory analysis support our assumptions on combined O_3 and RH as tracers to identify local and non-local air masses in the 5–10 km altitude range. They further allow conclusions on air mass origin, frequency of occurrence and controlling processes. Seasonal variability in O_3 VMR, RH and the vertical movement already separate

510 between pathways to the TWP and air mass origin. The additional quantitative tracer anomaly categorization emphasizes the link between air mass origin and tracer variability directly tied to different processes.

The two quantitative air mass categories $\Delta O_3 \circ \Delta RH \circ$ and $\Delta O_3 + \Delta RH$- can be related to the two governing transport patterns for Palau mid-tropospheric air masses, the clean Pacific and the polluted anticyclonic pathway (Fig. 11). The anticyclonic route for $\Delta O_3 + \Delta RH$- air masses occurs particularly during FMA. These air masses originate in tropical South East Asia,

515 where biomass burning is a potent source of pollution (e.g., Anderson et al., 2016; Yadav et al., 2017; Ogino et al., 2022).

They experience large-scale clear-sky subsidence associated with the Hadley circulation and dehydration during their transport within the tropical troposphere (Dessler and Minschwaner, 2007; Anderson et al., 2016). The PV values along the 10 days backward trajectories remain below 1.5 PVU (with some very rare exceptions). That means, that they do not originate in the extra-tropical stratosphere, which is characterized by PV values above 1.5 PVU. During ASO, these air masses are missing and we therefore see the undisturbed, extremely ozone-poor background (Fig. 8a). The $\Delta O_3 \circ \Delta RH \circ$ background air masses ascend towards Palau, consistent with convective uplift. They do not leave the convectively active local Pacific region in the 10 days before arrival in Palau.

Within the debate on origin and genesis of O_3+RH- air masses in the TWP, our analysis therefore supports the results of Anderson et al. (2016), i.e. a tropospheric origin of O_3+RH- air. Other studies, some using the same data from the CONTRAST campaign as Anderson et al., come to the conclusion of a dominant stratospheric origin (e.g., Stoller et al., 1999; Hayashi et al., 2008; Randel et al., 2016; Tao et al., 2018). Tao et al. (2018) conducted a quantitative study of the origin of O_3+RH- layers for the CONTRAST campaign using an artificial stratospheric tracer in the Lagrangian transport model CLaMS. They found a stratospheric influence in 60% of O_3+RH- air masses due to in-mixing during isentropic transport and point out the limitations of calculating pure Lagrangian trajectories without chemistry. According to our analysis, the anticyclonic route identified for ΔO_3+ΔRH- air masses reaching Palau is indeed a pathway along the subtropical ridge, i.e. in close proximity to mid-latitude UTLS air masses. But a lack of air masses with high PV and the clustering of the trajectory ending points near centers of pollution sources on the ground are strong evidence for a tropical tropospheric origin. This is supported by the seasonality of ΔO_3+ΔRH- layers coinciding with the annual low in convective activity in FMA. We, however, cannot fully rule out a possible contribution of in-mixing of extratropical stratospheric air along the way to Palau. The additional use of aerosol observations from the co-located lidar instrument ComCAL and potentially more tracer observations during the ACCLIP campaign in late summer 2022 will contribute to the debate. Further insights are expected during the ongoing El Niño cycle with a potentially higher frequency of O_3+RH- air mass observations.

We propose biomass burning or anthropogenic pollution as a source of O_3 production in dry, ozone-rich layers at their remote origin. Their seasonal occurrence tied to the position of the Intertropical Convergence Zone indeed opens a pathway from potential source regions which is confirmed by the trajectory analysis. If the attribution to tropical biomass burning holds, this might become a strong argument for policy makers. Anderson et al. (2016) pointed out, that due to the contribution of tropospheric O_3 to radiative forcing, present legislation aiming at the limitation of O_3 precursor emissions in the extra-tropics might not be enough to mitigate climate change.

6 Conclusions

Our study sheds light on air mass transport to the TWP as a key region of stratospheric entry and sets a valuable contribution to the discussion about anomalous layers of dry ozone-rich air observed in ozone-poor background profiles in the TWP (e.g., Anderson et al., 2016; Randel et al., 2016; Tao et al., 2018). We complemented a seasonal and statistical analysis of the balloon-borne PAO O_3 and RH time series (2016-19) with Lagrangian backward trajectory calculations. This approach

allowed us to differentiate between air masses in the 5–10 km altitude range above Palau regarding their origin, frequency
and underlying processes. We conclude, that humid, ozone-poor ($\Delta O_3 \circ \Delta RH \circ$) air masses are of local or Pacific convective
origin and occur year-round, but dominate from August until October. Anomalously dry ozone-rich ($\Delta O_3 + \Delta RH$-) air origi-
nates in Tropical Asia and is subsequently transported to the TWP via an anticyclonic route, mostly from February to April.
The origin in Tropical Asia suggests different sources of ground pollution as a cause for high O_3 values. No evidence for a
potential stratospheric origin was found by investigating potential vorticity on the backward trajectories or by analyzing the
geographical distribution of their origin. We propose that large-scale descent within the tropical troposphere and subsequent
radiative cooling in connection with the Hadley circulation is responsible for the vertical displacement and dehydration. In the
future, an extended time series incorporating more ENSO cycles, coinciding measurements from the ACCLIP campaign and
aerosol observations by the co-located lidar system ComCAL will be applied to further validate the non-stratospheric origin of
anomalous layers.

Code and data availability. All code used to produce the data and results is available upon request. The ozonesonde dataset is available
under https://doi.org/10.5281/zenodo.6920648 and will be included in the SHADOZ database in the future. The trajectory dataset calculated
by ATLAS is available under https://doi.org/10.5281/zenodo.8038600. ECMWF ERA5 data used for trajectory modelling is accessible via
the Copernicus Climate Change Service Climate Data Store (CDS): https://cds.climate.copernicus.eu/.

Appendix A

565 Figures A1, A2, A3 and A4 all give detailed insight into the seasonal or monthly variability of O_3 VMR and RH measured at the PAO. The following Figs. A5, A6 and A8 refer to the anomaly categories $\Delta O_3 \Delta RH$ as defined in Sect. 3.1.3. Figure A7 shows data from the trajectory dataset for the seasons FMA and ASO.
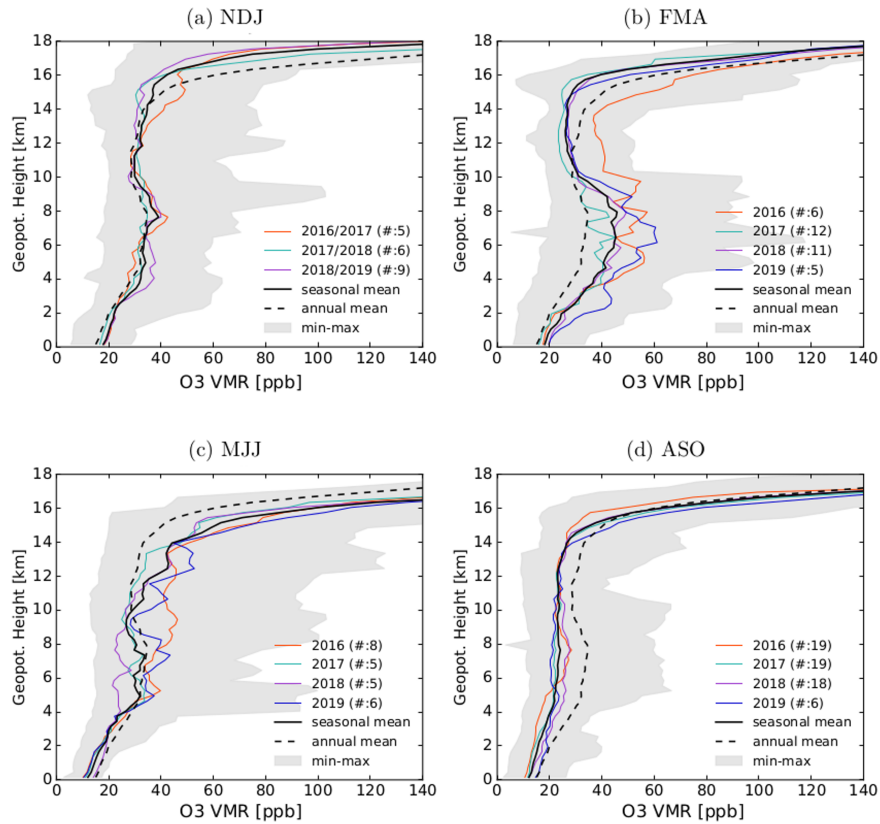
Figure A1. Variability of seasonal mean O_3 VMR profiles for Palau (black solid lines) in comparison to the long-term annual mean (dashed black line) in individual panels per season (a-d), all excluding the El Niño 2016 event, i.e. starting 08/2016; the grey shaded area encloses all observations, minimum to maximum, thin colored lines indicate seasonal means per year, number (#) of profiles included in the calculations given in brackets (compare Fig. 6).
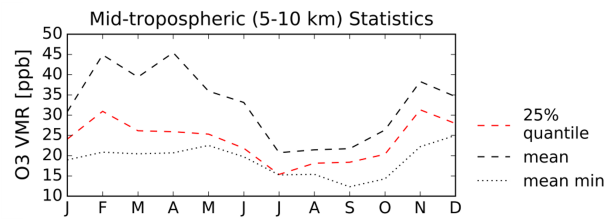
Figure A2. Statistical O_3 VMR measures for the 5–10 km altitude range highlighting the minimum O_3 season: monthly means from individual soundings' 25 % quantiles (red dashed line), mean (black dashed line) and minimum (black dotted line).
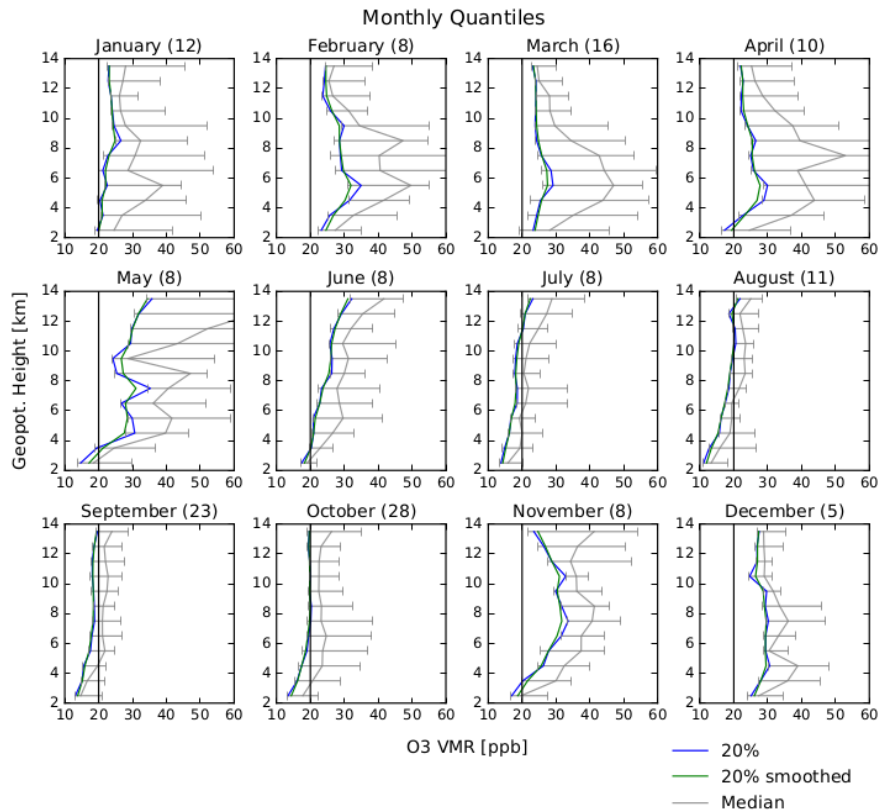
Figure A3. Monthly O_3 VMR statistics for Palau free tropospheric profiles as a function of altitude: 20th quantile (Q20) in blue, vertically smoothed using exponentially weighted averages in green, median in grey and central 66.6 % range in grey horizontal bars; number of included individual profiles in brackets, for orientation 20 ppb O_3 VMR is marked as a black vertical line (compare Figs. 4 and A4).
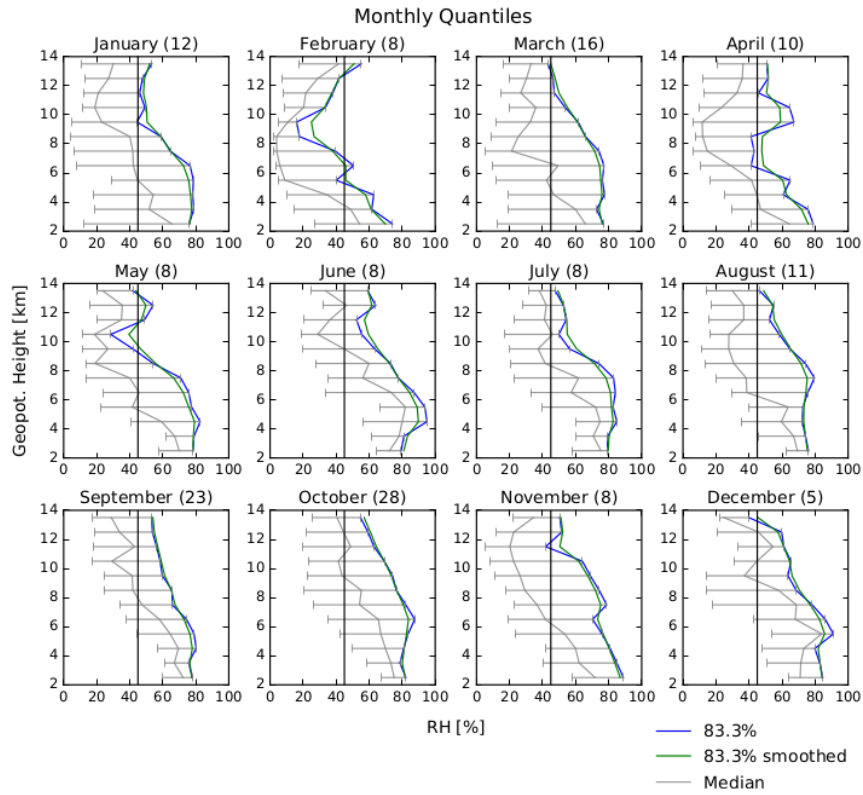
Figure A4. Monthly RH statistics for Palau free tropospheric profiles as a function of altitude: 83.3th quantile (Q83) in blue, for more details see Fig. A3; 45 % RH is highlighted by a black vertical line (compare Figs. 4 and A3).
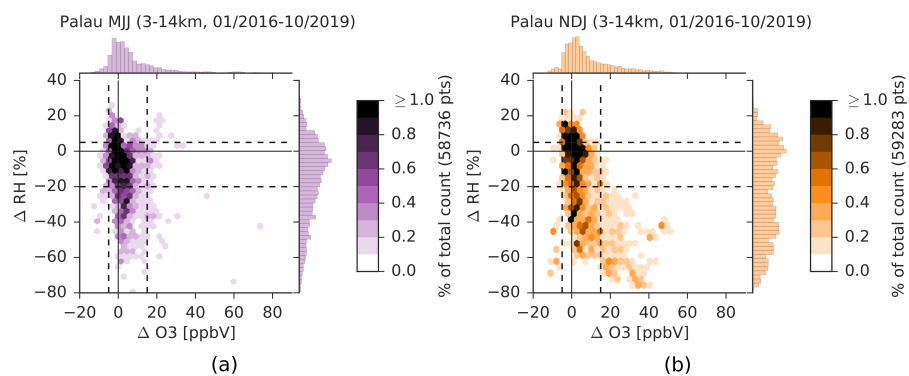
Figure A5. Seasonal free-tropospheric (3-14 km) relation between tracer anomalies ΔO_3 VMR and ΔRH for November-December-January (NDJ) (a) and May-June-July (MJJ) (b), colors according to Fig. 6, more details in Figs. 8 and 7.
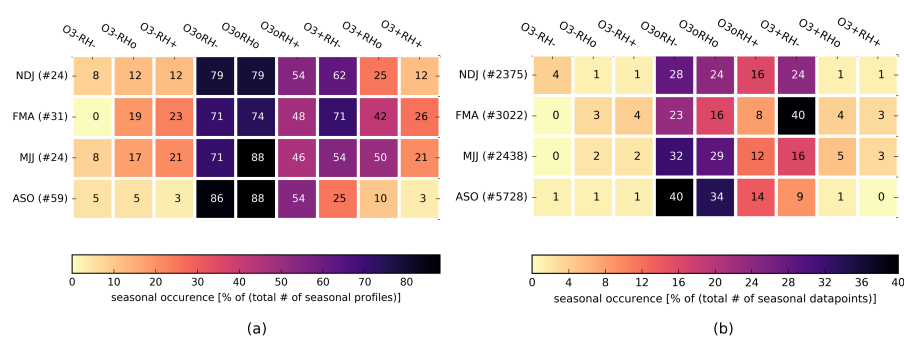
Figure A6. Heat map for the seasonal occurrence of air mass anomaly categories $\Delta O_3/\Delta RH$ based on the definition given in Sect. 3.1.3 and presented in Fig. 7 for Palau observations in the 5–10 km altitude range (trajectory dataset, see Sect. 2); panel (a) shows the occurrence relative to the total number (#) of seasonal profiles and panel (b) relative to the total number of all data points within the season; total numbers are given in brackets per season.

For the trajectory dataset in the 5–10 km altitude range, we observed $\Delta O_3 \circ \Delta RH \circ$ air masses in 74 % of FMA profiles and 88 % of ASO profiles (Fig. A6). $\Delta O_3 + \Delta RH$- air masses occur in 71 % of all individual FMA profiles and only 25 % of ASO profiles. In relation to the total number of seasonal data points, this contrast is even stronger: 40 % of all observed FMA data points and only 9 % of all ASO data points are identified as $\Delta O_3 + \Delta RH$- air.
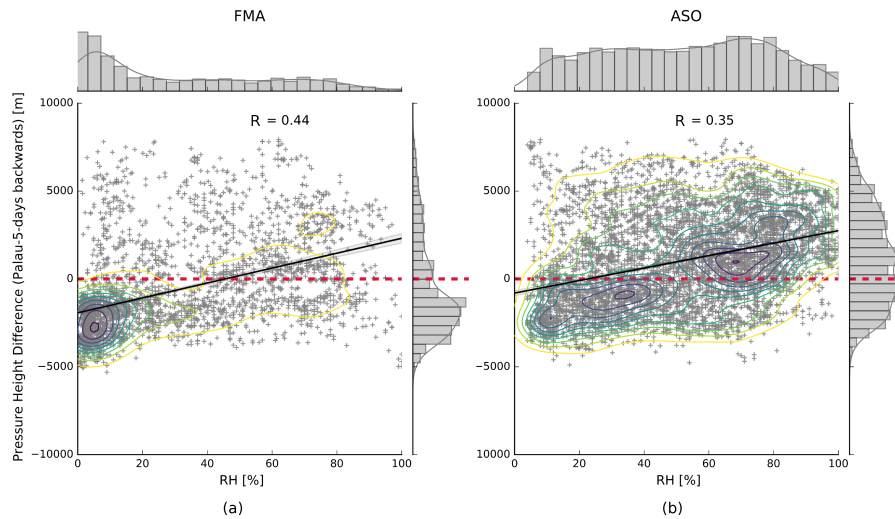
Figure A7. Relative humidity (RH) from observations above Palau versus difference in pressure altitude (between measurement date in Palau and five days before measurement) inferred from the backward trajectory analysis for the seasons FMA (a) and ASO (b); grey "+" indicate individual measurements from the trajectory dataset; colored contours show the distribution density; the black line indicates a fit by linear regression with a grey shaded 95 % confidence interval; the red dashed line highlights the zero line for the altitude difference with positive values indicating ascent and negative values descent towards Palau; the correlation coefficient R is shown in the plot; the marginal plots show univariate histograms and kernel-density estimated curves.

Figure A7 visualizes the correlation between RH and ascent/descent in a 2D histogram with a linear regression line. For FMA (Fig. A7a) the distribution reveals a cluster of very dry (<20 % RH) air masses that descended towards Palau (≈ 3 km). This cluster at the lower end of the physically possible scale is responsible for the low correlation between the two parameters, 575 which is surprisingly low despite the clear geographical separation visible in Fig. 10c.
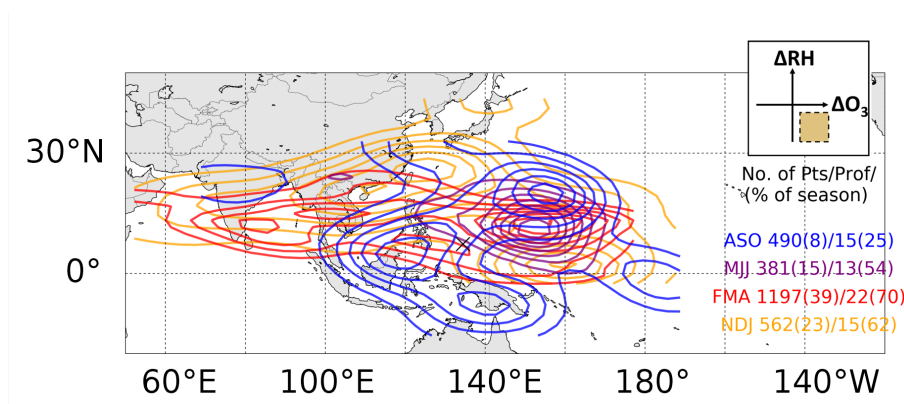
Figure A8. Seasonal distributions of the location of $\Delta O_3 + \Delta RH$- air masses five days before their measurement in Palau in the 5–10 km altitude range inferred from trajectories, according to the definition shown in Fig. 7; numbers in the plot from left to right: absolute number of individual air masses (trajectories) per season and as percentage per season in brackets, absolute number of profiles per season given and as percentage per season in brackets; differences to numbers shown in Fig. A6 due to rounding differences; see Fig. 6 for seasons.

Appendix B: Statistical Averages

There are different ways to derive a climatological seasonal average and choosing the best-suited definition is not trivial with our given data set. Data from an individual sounding are first averaged in 300 m height bins using an arithmetic mean (hereafter referred to as "mean"), which essentially complies with the vertical measurement resolution, introducing only a slightly greater degree of smoothing (cf. Müller et al., 2024). In the following temporal binning, the order of required steps must be considered as they lead to different values in our time series. There are four different possible sequences for (i) monthly, (ii) seasonal and (iii) annual averaging (Müller, 2020). In our case, we chose to first directly average individual profiles $x_i(m,y)$ of month m of all years y to a climatological month mean, climmonmean(m), then to a climatological season mean over all years, climseasmean(s):

$$\text{climmonmean}(m) = \frac{1}{\sum\limits_{y=1}^{Y} N(m,y)} * \sum_{y=1}^{Y} \sum_{i=1}^{N(m,y)} x_i(m,y) \tag{B1}$$

$$\text{climseasmean}(s) = \frac{1}{M(s)} * \sum_{i=1}^{M(s)} \text{climmonmean}(i), \tag{B2}$$

with $M(s)$ as the months in season s, $N(m,y)$ as the number of profiles in month m of year y and Y as the number of years. climseasmean(s) will not overestimate single months with very few and/or outlying profiles, assuming the interannual variability of the months is small compared to variations between different months.

Author contributions. KM wrote the original draft of this work and performed the analysis. PvdG and MR supported the analysis and provided effective and constructive comments to improve the manuscript. KM and others performed the measurements. All authors contributed to writing the paper.

Competing interests. None of the authors has any financial or personal relationships that could inappropriately influence or bias the content of the paper.

Acknowledgements. The setup of the PAO and this study was mostly funded by the European Union under the 7th Framework Program as part of the StratoClim project (www.stratoclim.org), grant number 603557. The authors thank Ingo Wohltmann (AWI) for support with the trajectory model and valuable feedback for the manuscript, Dr. Patrick Tellei, President of the Palau Community College, for provision of space, German Honorary Consul Thomas Schubert for overall support, and various people and institutions for operations at the PAO: Sharon Patris (CRRF), Pat and Lori Colin (CRRF), Gerda Ucharm (CRRF), Ingo Beninga (impres GmbH), Wilfried Ruhe (impres GmbH), Winfried Markert (Uni Bremen), Tine Weinzierl (formerly Uni Bremen), Jordis Tradowsky (NMet) and Jürgen "Egon" Graeser (AWI). The authors

want to further thank Herman Smit (FZJ), Ross Salawitch (UMD), Laura Pan (NCAR), Anne Thompson (NASA/GSFC) and many others from the international ozone research community for discussions and encouragement. Finally, the authors thank two anonymous reviewers for providing valuable comments and thus improving the manuscript.

605 **References**

Anderson, D. C., Nicely, J. M., Salawitch, R. J., Canty, T. P., Dickerson, R. R., Hanisco, T. F., Wolfe, G. M., Apel, E. C., Atlas, E., Bannan, T., Bauguitte, S., Blake, N. J., Bresch, J. F., Campos, T. L., Carpenter, L. J., Cohen, M. D., Evans, M., Fernandez, R. P., Kahn, B. H., Kinnison, D. E., Hall, S. R., Harris, N. R., Hornbrook, R. S., Lamarque, J.-F., Le Breton, M., Lee, J. D., Percival, C., Pfister, L., Pierce, R. B., Riemer, D. D., Saiz-Lopez, A., Stunder, B. J., Thompson, A. M., Ullmann, K., Vaughan, A., and Weinheimer, A. J.: A Pervasive Role for Biomass
610   Burning in Tropical High Ozone/Low Water Structures, Nature Communications, 7, 10 267, https://doi.org/10.1038/ncomms10267, 2016.

Bozem, H., Butler, T. M., Lawrence, M. G., Harder, H., Martinez, M., Kubistin, D., Lelieveld, J., and Fischer, H.: Chemical Processes Related to Net Ozone Tendencies in the Free Troposphere, Atmospheric Chemistry and Physics, 17, 10 565–10 582, https://doi.org/10.5194/acp-17-10565-2017, 2017.

Browell, E. V., Fenn, M. A., Butler, C. F., Grant, W. B., Ismail, S., Ferrare, R. A., Kooi, S. A., Brackett, V. G., Clayton, M. B., Avery, M. A.,
615   Barrick, J. D. W., Fuelberg, H. E., Maloney, J. C., Newell, R. E., Zhu, Y., Mahoney, M. J., Anderson, B. E., Blake, D. R., Brune, W. H., Heikes, B. G., Sachse, G. W., Singh, H. B., and Talbot, R. W.: Large-scale Air Mass Characteristics Observed over the Remote Tropical Pacific Ocean during March-April 1999: Results from PEM-Tropics B Field Experiment, Journal of Geophysical Research: Atmospheres, 106, 32 481–32 501, https://doi.org/10.1029/2001JD900001@10.1002/(ISSN)2169-8996.PEMTROP2, 2001.

Cau, P., Methven, J., and Hoskins, B.: Origins of Dry Air in the Tropics and Subtropics, Journal of Climate, 20, 2745–2759,
620   https://doi.org/10.1175/JCLI4176.1, 2007.

Cecil, D. J., Buechler, D. E., and Blakeslee, R. J.: Gridded Lightning Climatology from TRMM-LIS and OTD: Dataset Description, Atmospheric Research, 135–136, 404–414, https://doi.org/10.1016/j.atmosres.2012.06.028, 2014.

Christian, H. J.: Global Frequency and Distribution of Lightning as Observed from Space by the Optical Transient Detector, Journal of Geophysical Research, 108, 4005, https://doi.org/10.1029/2002JD002347, 2003.

625 Crawford, J. H., Davis, D. D., Chen, G., Bradshaw, J., Sandholm, S., Kondo, Y., Merrill, J., Liu, S., Browell, E., Gregory, G., Anderson, B., Sachse, G., Barrick, J., Blake, D., Talbot, R., and Pueschel, R.: Implications of Large Scale Shifts in Tropospheric NO$_x$ Levels in the Remote Tropical Pacific, Journal of Geophysical Research: Atmospheres, 102, 28 447–28 468, https://doi.org/10.1029/97JD00011, 1997.

Dessler, A. E. and Minschwaner, K.: An Analysis of the Regulation of Tropical Tropospheric Water Vapor, Journal of Geophysical Research: Atmospheres, 112, https://doi.org/10.1029/2006JD007683, 2007.

630 Diallo, M., Riese, M., Birner, T., Konopka, P., Müller, R., Hegglin, M. I., Santee, M. L., Baldwin, M., Legras, B., and Ploeger, F.: Response of Stratospheric Water Vapor and Ozone to the Unusual Timing of El Niño and the QBO Disruption in 2015–2016, Atmospheric Chemistry and Physics, 18, 13 055–13 073, https://doi.org/10.5194/acp-18-13055-2018, 2018.

Dima, I. M., Wallace, J., M., and Kraucunas, I.: Tropical Zonal Momentum Balance in the NCEP Reanalyses, Journal of the Atmospheric Sciences, 62, 2499 – 2513, https://doi.org/10.1175/JAS3486.1, 2005.

635 Folkins, I.: Tropical Ozone as an Indicator of Deep Convection, Journal of Geophysical Research, 107, 4184, https://doi.org/10.1029/2001JD001178, 2002.

Folkins, I. and Martin, R. V.: The Vertical Structure of Tropical Convection and Its Impact on the Budgets of Water Vapor and Ozone, Journal of the Atmospheric Sciences, 62, 1560–1573, https://doi.org/10.1175/JAS3407.1, 2005.

Fueglistaler, S., Wernli, H., and Peter, T.: Tropical Troposphere-to-Stratosphere Transport Inferred from Trajectory Calculations, Journal of
640   Geophysical Research: Atmospheres, 109, https://doi.org/10.1029/2003JD004069, 2004.

Gettelman, A. and Forster, P. d. F.: A Climatology of the Tropical Tropopause Layer., Journal of the Meteorological Society of Japan, 80, 911–924, https://doi.org/10.2151/jmsj.80.911, 2002.

Gettelman, A., Lauritzen, P. H., Park, M., and Kay, J. E.: Processes Regulating Short-Lived Species in the Tropical Tropopause Layer, Journal of Geophysical Research, 114, D13 303, https://doi.org/10.1029/2009JD011785, 2009.

645 Gill, A. E.: Some simple solutions for heat-induced tropical circulation, Quarterly Journal of the Royal Meteorological Society, 106, 447–462, 1980.

Harris, N. R. P., Carpenter, L. J., Lee, J. D., Vaughan, G., Filus, M. T., Jones, R. L., OuYang, B., Pyle, J. A., Robinson, A. D., Andrews, S. J., Lewis, A. C., Minaeian, J., Vaughan, A., Dorsey, J. R., Gallagher, M. W., Le Breton, M., Newton, R., Percival, C. J., Ricketts, H. M. A., Bauguitte, S. J.-B., Nott, G. J., Wellpott, A., Ashfold, M. J., Flemming, J., Butler, R., Palmer, P. I., Kaye, P. H., Stopford, C.,

650 Chemel, C., Boesch, H., Humpage, N., Vick, A., MacKenzie, A. R., Hyde, R., Angelov, P., Meneguz, E., and Manning, A. J.: Coordinated Airborne Studies in the Tropics (CAST), Bulletin of the American Meteorological Society, 98, 145–162, https://doi.org/10.1175/BAMS-D-14-00290.1, 2017.

Hayashi, H., Kita, K., and Taguchi, S.: Ozone-Enhanced Layers in the Troposphere over the Equatorial Pacific Ocean and the Influence of Transport of Midlatitude UT/LS Air, Atmospheric Chemistry and Physics, p. 14, 2008.

655 Hersbach, H., Bell, B., Berrisford, P., Hirahara, S., Horányi, A., Muñoz-Sabater, J., Nicolas, J., Peubey, C., Radu, R., Schepers, D., Simmons, A., Soci, C., Abdalla, S., Abellan, X., Balsamo, G., Bechtold, P., Biavati, G., Bidlot, J., Bonavita, M., Chiara, G., Dahlgren, P., Dee, D., Diamantakis, M., Dragani, R., Flemming, J., Forbes, R., Fuentes, M., Geer, A., Haimberger, L., Healy, S., Hogan, R. J., Hólm, E., Janisková, M., Keeley, S., Laloyaux, P., Lopez, P., Lupu, C., Radnoti, G., Rosnay, P., Rozum, I., Vamborg, F., Villaume, S., and Thépaut, J.-N.: The ERA5 Global Reanalysis, Quarterly Journal of the Royal Meteorological Society, 146, 1999–2049, https://doi.org/10.1002/qj.3803, 2020.

660 Huang, B., L'Heureux, M., Hu, Z.-Z., and Zhang, H.-M.: Ranking the Strongest ENSO Events While Incorporating SST Uncertainty, Geophysical Research Letters, 43, 9165–9172, 2016.

Kley, D., Crutzen, P. J., Smit, H. G. J., Vomel, H., Oltmans, S. J., Grassl, H., and Ramanathan, V.: Observations of Near-Zero Ozone Concentrations Over the Convective Pacific: Effects on Air Chemistry, Science, 274, 230–233, https://doi.org/10.1126/science.274.5285.230, 1996.

665 Kley, D., Smit, H. G. J., Vömel, H., Grassl, H., Ramanathan, V., Crutzen, P. J., Williams, S., Meywerk, J., and Oltmans, S. J.: Tropospheric Water-Vapour and Ozone Cross-Sections in a Zonal Plane over the Central Equatorial Pacific Ocean, Quarterly Journal of the Royal Meteorological Society, 123, 2009–2040, https://doi.org/10.1002/qj.49712354312, 1997.

Komhyr, W. D.: Electrical Concentration Cells for Gas Analysis, Annales Geophysicae, 25, 203–210, 1969.

Krüger, K. and Quack, B.: Introduction to Special Issue: The TransBrom Sonne Expedition in the Tropical West Pacific, Atmospheric

670 Chemistry and Physics, 13, 9439–9446, https://doi.org/10.5194/acp-13-9439-2013, 2013.

Krüger, K., Tegtmeier, S., and Rex, M.: Long-Term Climatology of Air Mass Transport through the Tropical Tropopause Layer (TTL) during NH Winter, Atmospheric Chemistry and Physics, 8, 813–823, https://doi.org/10.5194/acp-8-813-2008, 2008.

Kunz, A., Konopka, P., Müller, R., and Pan, L. L.: Dynamical Tropopause Based on Isentropic Potential Vorticity Gradients, Journal of Geophysical Research, 116, D01 110, https://doi.org/10.1029/2010JD014343, 2011.

675 Levy, H.: Normal Atmosphere: Large Radical and Formaldehyde Concentrations Predicted, Science, 173, 141–143, https://doi.org/10.1126/science.173.3992.141, 1971.

Liu, S. C., McFarland, M., Kley, D., Zafiriou, O., and Huebert, B.: Tropospheric NO_x and O_3 Budgets in the Equatorial Pacific, Journal of Geophysical Research, 88, 1360, https://doi.org/10.1029/JC088iC02p01360, 1983.

Mapes, B. E.: Water's Two Height Scales: The Moist Adiabat and the Radiative Troposphere, Quarterly Journal of the Royal Meteorological Society, 127, 2353–2366, https://doi.org/10.1002/qj.49712757708, 2001.

Mapes, B. E. and Zuidema, P.: Radiative-Dynamical Consequences of Dry Tongues in the Tropical Troposphere, Journal of the Atmospheric Sciences, 53, 620–638, https://doi.org/10.1175/1520-0469(1996)053<0620:RDCODT>2.0.CO;2, 1996.

Matsuno, T.: Quasi-geostrophic motions in the equatorial area, Journal of the Meteorological Society of Japan. Ser. II, 44, 25–43, 1966.

Müller, K.: Characterization of Ozone and the Oxidizing Capacity of the Tropical West Pacific Troposphere, Ph.D. thesis, Universität Bremen, https://doi.org/10.26092/ELIB/463, 2020.

Müller, K., Tradowsky, J. S., von der Gathen, P., Ritter, C., Patris, S., Notholt, J., and Rex, M.: Measurement Report: The Palau Atmospheric Observatory and its ozonesonde record – continuous monitoring of tropospheric composition and dynamics in the tropical western Pacific, Atmospheric Chemistry and Physics, 24, 2169–2193, https://doi.org/10.5194/acp-24-2169-2024, 2024.

Newell, R. E. and Gould-Stewart, S.: A Stratospheric Fountain?, Journal of the Atmospheric Sciences, 38, 2789–2796, 1981.

Newell, R. E., Zhu, Y., Browell, E. V., Ismail, S., Read, W. G., Waters, J. W., Kelly, K. K., and Liu, S. C.: Upper Tropospheric Water Vapor and Cirrus: Comparison of DC-8 Observations, Preliminary UARS Microwave Limb Sounder Measurements and Meteorological Analyses, Journal of Geophysical Research: Atmospheres, 101, 1931–1941, 1996.

Newell, R. E., Thouret, V., Cho, J. Y. N., Stoller, P., Marenco, A., and Smit, H. G.: Ubiquity of Quasi-Horizontal Layers in the Troposphere, Nature, 398, 316–319, https://doi.org/10.1038/18642, 1999.

Newton, R., Vaughan, G., Ricketts, H. M. A., Pan, L. L., Weinheimer, A. J., and Chemel, C.: Ozonesonde Profiles from the West Pacific Warm Pool: Measurements and Validation, Atmospheric Chemistry and Physics, 16, 619–634, https://doi.org/10.5194/acp-16-619-2016, 2016.

Nicely, J. M., Anderson, D. C., Canty, T. P., Salawitch, R. J., Wolfe, G. M., Apel, E. C., Arnold, S. R., Atlas, E. L., Blake, N. J., Bresch, J. F., Campos, T. L., Dickerson, R. R., Duncan, B., Emmons, L. K., Evans, M. J., Fernandez, R. P., Flemming, J., Hall, S. R., Hanisco, T. F., Honomichl, S. B., Hornbrook, R. S., Huijnen, V., Kaser, L., Kinnison, D. E., Lamarque, J.-F., Mao, J., Monks, S. A., Montzka, D. D., Pan, L. L., Riemer, D. D., Saiz-Lopez, A., Steenrod, S. D., Stell, M. H., Tilmes, S., Turquety, S., Ullmann, K., and Weinheimer, A. J.: An Observationally Constrained Evaluation of the Oxidative Capacity in the Tropical Western Pacific Troposphere: Observationally Constrained OH in TWP, Journal of Geophysical Research: Atmospheres, 121, 7461–7488, https://doi.org/10.1002/2016JD025067, 2016.

Ogino, S.-Y., Fujiwara, M., Shiotani, M., Hasebe, F., Matsumoto, J., T. Hoang, T. H., and T. Nguyen, T. T.: Ozone Variations over the Northern Subtropical Region Revealed by Ozonesonde Observations in Hanoi, Journal of Geophysical Research: Atmospheres, 118, 3245–3257, https://doi.org/10.1002/jgrd.50348, 2013.

Ogino, S.-Y., Miyazaki, K., Fujiwara, M., Nodzu, M. I., Shiotani, M., Hasebe, F., Matsumoto, J., Witte, J., Thompson, A. M., Nguyen-Thi, H. A., and Nguyen, T. V.: Cause of a Lower-Tropospheric High-Ozone Layer in Spring Over Hanoi, Journal of Geophysical Research: Atmospheres, 127, e2021JD035 727, https://doi.org/https://doi.org/10.1029/2021JD035727, e2021JD035727 2021JD035727, 2022.

Oltmans, S. J., Johnson, B. J., Harris, J. M., Vömel, H., Thompson, A. M., Koshy, K., Simon, P., Bendura, R. J., Logan, J. A., Hasebe, F., Shiotani, M., Kirchhoff, V. W. J. H., Maata, M., Sami, G., Samad, A., Tabuadravu, J., Enriquez, H., Agama, M., Cornejo, J., and Paredes, F.: Ozone in the Pacific Tropical Troposphere from Ozonesonde Observations, Journal of Geophysical Research: Atmospheres, 106, 32 503–32 525, https://doi.org/10.1029/2000JD900834@10.1002/(ISSN)2169-8996.PEMTROP2, 2001.

Pan, L. L., Paulik, L. C., Honomichl, S. B., Munchak, L. A., Bian, J., Selkirk, H. B., and Vömel, H.: Identification of the Tropical Tropopause Transition Layer Using the Ozone-Water Vapor Relationship, Journal of Geophysical Research: Atmospheres, 119, 3586–3599, https://doi.org/10.1002/2013JD020558, 2014.

Pan, L. L., Honomichl, S. B., Randel, W. J., Apel, E. C., Atlas, E. L., Beaton, S. P., Bresch, J. F., Hornbrook, R., Kinnison, D. E., Lamarque, J.-F., Saiz-Lopez, A., Salawitch, R. J., and Weinheimer, A. J.: Bimodal Distribution of Free Tropospheric Ozone over the Tropical Western Pacific Revealed by Airborne Observations, Geophysical Research Letters, 42, 7844–7851, https://doi.org/10.1002/2015GL065562, 2015.

Pan, L. L., Atlas, E. L., Salawitch, R. J., Honomichl, S. B., Bresch, J. F., Randel, W. J., Apel, E. C., Hornbrook, R. S., Weinheimer, A. J., Anderson, D. C., Andrews, S. J., Baidar, S., Beaton, S. P., Campos, T. L., Carpenter, L. J., Chen, D., Dix, B., Donets, V., Hall, S. R., Hanisco, T. F., Homeyer, C. R., Huey, L. G., Jensen, J. B., Kaser, L., Kinnison, D. E., Koenig, T. K., Lamarque, J.-F., Liu, C., Luo, J., Luo, Z. J., Montzka, D. D., Nicely, J. M., Pierce, R. B., Riemer, D. D., Robinson, T., Romashkin, P., Saiz-Lopez, A., Schauffler, S., Shieh, O., Stell, M. H., Ullmann, K., Vaughan, G., Volkamer, R., and Wolfe, G.: The Convective Transport of Active Species in the Tropics (CONTRAST) Experiment, Bulletin of the American Meteorological Society, 98, 106–128, https://doi.org/10.1175/BAMS-D-14-00272.1, 2017.

Paulik, L. C. and Birner, T.: Quantifying the Deep Convective Temperature Signal within the Tropical Tropopause Layer (TTL), Atmospheric Chemistry and Physics, 12, 12 183–12 195, https://doi.org/10.5194/acp-12-12183-2012, 2012.

Ploeger, F., Fueglistaler, S., Grooß, J.-U., Günther, G., Konopka, P., Liu, Y., Müller, R., Ravegnani, F., Schiller, C., Ulanovski, A., and Riese, M.: Insight from Ozone and Water Vapour on Transport in the Tropical Tropopause Layer (TTL), Atmospheric Chemistry and Physics, 11, 407–419, https://doi.org/10.5194/acp-11-407-2011, 2011.

Randel, W. J., Park, M., Wu, F., and Livesey, N.: A Large Annual Cycle in Ozone above the Tropical Tropopause Linked to the Brewer–Dobson Circulation, Journal of the Atmospheric Sciences, 64, 4479–4488, https://doi.org/10.1175/2007JAS2409.1, 2007.

Randel, W. J., Rivoire, L., Pan, L. L., and Honomichl, S. B.: Dry Layers in the Tropical Troposphere Observed during CONTRAST and Global Behavior from GFS Analyses: Dry Layers in the Tropical Troposphere, Journal of Geophysical Research: Atmospheres, 121, 14,142–14,158, https://doi.org/10.1002/2016JD025841, 2016.

Rex, M., Wohltmann, I., Ridder, T., Lehmann, R., Rosenlof, K., Wennberg, P., Weisenstein, D., Notholt, J., Krüger, K., Mohr, V., and Tegtmeier, S.: A Tropical West Pacific OH Minimum and Implications for Stratospheric Composition, Atmospheric Chemistry and Physics, 14, 4827–4841, https://doi.org/10.5194/acp-14-4827-2014, 2014.

Ruzmaikin, A., Aumann, H. H., and Manning, E. M.: Relative Humidity in the Troposphere with AIRS, Journal of the Atmospheric Sciences, 71, 2516 – 2533, https://doi.org/10.1175/JAS-D-13-0363.1, 2014.

Schoeberl, M. R., Selkirk, H. B., Vömel, H., and Douglass, A. R.: Sources of Seasonal Variability in Tropical Upper Troposphere and Lower Stratosphere Water Vapor and Ozone: Inferences from the Ticosonde Data Set at Costa Rica, Journal of Geophysical Research: Atmospheres, 120, 9684–9701, https://doi.org/10.1002/2015JD023299, 2015.

Sherwood, S. C., Kursinski, E. R., and Read, W. G.: A Distribution Law for Free-Tropospheric Relative Humidity, Journal of Climate, 19, 6267 – 6277, https://doi.org/10.1175/JCLI3978.1, 2006.

Sherwood, S. C., Roca, R., Weckwerth, T. M., and Andronova, N. G.: Tropospheric Water Vapor, Convection, and Climate, Reviews of Geophysics, 48, 1, https://doi.org/10.1029/2009RG000301, 2010.

Smit, H. and Thompson, A.: Ozonesonde Measurement Principles and Best Operational Practices: ASOPOS 2.0 (Assessment of Standard Operating Procedures for Ozonesondes), WMO, World Meteorological Organization, GAW Report, p. 173, 2021.

Smit, H. G. J.: Quality Assurance and Quality Control for Ozonesonde Measurements in GAW, GAW Report No. 201, WMO, 2014.

Solomon, S., Thompson, D. W. J., Portmann, R. W., Oltmans, S. J., and Thompson, A. M.: On the Distribution and Variability of Ozone in the Tropical Upper Troposphere: Implications for Tropical Deep Convection and Chemical-Dynamical Coupling, Geophysical Research Letters, 32, L23 813, https://doi.org/10.1029/2005GL024323, 2005.

755   Stauffer, R. M., Thompson, A. M., and Witte, J. C.: Characterizing Global Ozonesonde Profile Variability From Surface to the UT/LS With a Clustering Technique and MERRA-2 Reanalysis, Journal of Geophysical Research: Atmospheres, 123, 6213–6229, https://doi.org/10.1029/2018JD028465, 2018.

Stoller, P., Cho, J. Y. N., Newell, R. E., Thouret, V., Zhu, Y., Carroll, M. A., Albercook, G. M., Anderson, B. E., Barrick, J. D. W., Browell, E. V., Gregory, G. L., Sachse, G. W., Vay, S., Bradshaw, J. D., and Sandholm, S.: Measurements of Atmospheric Layers
760   from the NASA DC-8 and P-3B Aircraft during PEM-Tropics A, Journal of Geophysical Research: Atmospheres, 104, 5745–5764, https://doi.org/10.1029/98JD02717, 1999.

Sun, X., Palm, M., Müller, K., Hachmeister, J., and Notholt, J.: Determination of the Chemical Equator from GEOS-Chem Model Simulation: A Focus on the Tropical Western Pacific Region, Atmospheric Chemistry and Physics, 23, 7075–7090, https://doi.org/10.5194/acp-23-7075-2023, 2023.

765   Takashima, H., Shiotani, M., Fujiwara, M., Nishi, N., and Hasebe, F.: Ozonesonde Observations at Christmas Island (2°N, 157°W) in the Equatorial Central Pacific, Journal of Geophysical Research, 113, D10 112, https://doi.org/10.1029/2007JD009374, 2008.

Tao, M., Pan, L. L., Konopka, P., Honomichl, S. B., Kinnison, D. E., and Apel, E. C.: A Lagrangian Model Diagnosis of Stratospheric Contributions to Tropical Midtropospheric Air, Journal of Geophysical Research: Atmospheres, 123, 9764–9785, https://doi.org/10.1029/2018JD028696, 2018.

770   Thompson, A. M., Tao, W.-K., Pickering, K. E., Scala, J. R., and Simpson, J.: Tropical Deep Convection and Ozone Formation, Bulletin of the American Meteorological Society, 78, 1043–1054, https://doi.org/10.1175/1520-0477(1997)078<1043:TDCAOF>2.0.CO;2, 1997.

Thompson, A. M., Witte, J. C., McPeters, R. D., Oltmans, S. J., Schmidlin, F. J., Logan, J. A., Fujiwara, M., Kirchhoff, V. W. J. H., Posny, F., Coetzee, G. J. R., Hoegger, B., Kawakami, S., Toshihiro, O., Johnson, B. J., Vömel, H., and Labow, G. J.: Southern Hemisphere Additional Ozonesondes (SHADOZ) 1998–2000 Tropical Ozone Climatology 1. Comparison with Total Ozone Mapping Spectrometer (TOMS) and
775   Ground-Based Measurements, Journal of Geophysical Research, 108, 8238, https://doi.org/10.1029/2001JD000967, 2003a.

Thompson, A. M., Witte, J. C., Oltmans, S. J., Schmidlin, F. J., Logan, J. A., Fujiwara, M., Kirchhoff, V. W. J. H., Posny, F., Coetzee, G. J. R., Hoegger, B., Kawakami, S., Ogawa, T., Fortuin, J. P. F., and Kelder, H. M.: Southern Hemisphere Additional Ozonesondes (SHADOZ) 1998–2000 Tropical Ozone Climatology 2. Tropospheric Variability and the Zonal Wave-One, Journal of Geophysical Research, 108, 8241, https://doi.org/10.1029/2002JD002241, 2003b.

780   Thompson, A. M., Miller, S. K., Tilmes, S., Kollonige, D. W., Witte, J. C., Oltmans, S. J., Johnson, B. J., Fujiwara, M., Schmidlin, F. J., Coetzee, G. J. R., Komala, N., Maata, M., bt Mohamad, M., Nguyo, J., Mutai, C., Ogino, S.-Y., Da Silva, F. R., Leme, N. M. P., Posny, F., Scheele, R., Selkirk, H. B., Shiotani, M., Stübi, R., Levrat, G., Calpini, B., Thouret, V., Tsuruta, H., Canossa, J. V., Vömel, H., Yonemura, S., Diaz, J. A., Tan Thanh, N. T., and Thuy Ha, H. T.: Southern Hemisphere Additional Ozonesondes (SHADOZ) Ozone Climatology (2005-2009): Tropospheric and Tropical Tropopause Layer (TTL) Profiles with Comparisons to OMI-based Ozone Products: SHADOZ
785   OZONE DURING AURA, Journal of Geophysical Research: Atmospheres, 117, n/a–n/a, https://doi.org/10.1029/2011JD016911, 2012.

Thompson, A. M., Witte, J. C., Sterling, C., Jordan, A., Johnson, B. J., Oltmans, S. J., Fujiwara, M., Vömel, H., Allaart, M., Piters, A., Coetzee, G. J. R., Posny, F., Corrales, E., Diaz, J. A., Félix, C., Komala, N., Lai, N., Ahn Nguyen, H. T., Maata, M., Mani, F., Zainal, Z., Ogino, S.-y., Paredes, F., Penha, T. L. B., Silva, F. R., Sallons-Mitro, S., Selkirk, H. B., Schmidlin, F. J., Stübi, R., and Thiongo, K.: First Reprocessing of Southern Hemisphere Additional Ozonesondes (SHADOZ) Ozone Profiles (1998–2016): 2. Comparisons With Satellites
790   and Ground-Based Instruments, Journal of Geophysical Research: Atmospheres, 122, https://doi.org/10.1002/2017JD027406, 2017.

Thompson, A. M., Smit, H. G. J., Witte, J. C., Stauffer, R. M., Johnson, B. J., Morris, G., von der Gathen, P., Van Malderen, R., Davies, J., Piters, A., Allaart, M., Posny, F., Kivi, R., Cullis, P., Hoang Anh, N. T., Corrales, E., Machinini, T., da Silva, F. R., Paiman, G., Thiong'o,

K., Zainal, Z., Brothers, G. B., Wolff, K. R., Nakano, T., Stübi, R., Romanens, G., Coetzee, G. J. R., Diaz, J. A., Mitro, S., Mohamad, M., and Ogino, S.-Y.: Ozonesonde Quality Assurance: The JOSIE–SHADOZ (2017) Experience, Bulletin of the American Meteorological Society, 100, 155–171, https://doi.org/10.1175/BAMS-D-17-0311.1, 2019.

Thompson, A. M., Stauffer, R. M., Wargan, K., Witte, J. C., Kollonige, D. E., and Ziemke, J. R.: Regional and Seasonal Trends in Tropical Ozone From SHADOZ Profiles: Reference for Models and Satellite Products, Journal of Geophysical Research: Atmospheres, 126, https://doi.org/10.1029/2021JD034691, 2021.

Thouret, V., Cho, J. Y. N., Newell, R. E., Marenco, A., and Smit, H. G. J.: General Characteristics of Tropospheric Trace Constituent Layers Observed in the MOZAIC Program, Journal of Geophysical Research: Atmospheres, 105, 17 379–17 392, https://doi.org/10.1029/2000JD900238, 2000.

Van Tuyl, A. H.: Advective influences on forced tropical motions, Journal of the atmospheric sciences, 43, 141–161, 1986.

Waugh, D. W. and Polvani, L. M.: Climatology of Intrusions into the Tropical Upper Troposphere, Geophysical Research Letters, 27, 3857–3860, https://doi.org/10.1029/2000GL012250, 2000.

Wohltmann, I. and Rex, M.: The Lagrangian Chemistry and Transport Model ATLAS: Validation of Advective Transport and Mixing, Geoscientific Model Development, 2, 153–173, https://doi.org/10.5194/gmd-2-153-2009, 2009.

Wohltmann, I., Lehmann, R., and Rex, M.: The Lagrangian Chemistry and Transport Model ATLAS: Simulation and Validation of Stratospheric Chemistry and Ozone Loss in the Winter 1999/2000, Geoscientific Model Development, 3, 585–601, https://doi.org/10.5194/gmd-3-585-2010, 2010.

Yadav, I. C., Linthoingambi Devi, N., Li, J., Syed, J. H., Zhang, G., and Watanabe, H.: Biomass burning in Indo-China peninsula and its impacts on regional air quality and global climate change - a review, Environmental Pollution, 227, 414–427, https://doi.org/https://doi.org/10.1016/j.envpol.2017.04.085, 2017.

Yoneyama, K. and Parsons, D. B.: A Proposed Mechanism for the Intrusion of Dry Air into the Tropical Western Pacific Region, Journal of the Atmospheric Sciences, 56, 1524–1546, https://doi.org/10.1175/1520-0469(1999)056<1524:APMFTI>2.0.CO;2, 1999.

Zhang, C., Mapes, B. E., and Soden, B. J.: Bimodality in tropical water vapour, Quarterly Journal of the Royal Meteorological Society, 129, 2847–2866, https://doi.org/https://doi.org/10.1256/qj.02.166, 2003.